https://doi.org/10.1016/j.energy.2023.128584

Energy harvesting based on flow-induced vibration of a wavy cylinder coupled with tuned mass damper

Fuwang Zhao[1,2,3 #], Zhaokun Wang[2 #], Honglei Bai[1 *], Hui Tang[2 *]

[1] *School of Aeronautics and Astronautics, Sun Yat-Sen University, Shenzhen Campus, Shenzhen 518107, China*

[2]*Research Center for Fluid-Structure Interactions, Department of Mechanical Engineering, The Hong Kong Polytechnic University, Kowloon, Hong Kong SAR, China*

[3]*School of Fashion and Textiles, The Hong Kong Polytechnic University, Kowloon, Hong Kong, China*

[#]These authors contributed equally to this work

*Corresponding author: baihlei3@mail.sysu.edu.cn, h.tang@polyu.edu.hk

Abstract

We investigate the flow-energy harvesting performance of a system consisting of a wavy cylinder and a tuned mass damper (TMD), through experiments, theoretical modelling and CFD simulations. The wavy cylinder is elastically supported, being able to oscillate transversally in cross flows and further enforcing a piezoelectric sheet to generate electricity. Results indicate that the output power strongly depends on wavelength λ_z, amplitude a, and the tip mass of TMD. The wavy cylinder outperforms the smooth cylinder when $\lambda_z \geq 3.6D_m$ and peaks at $\lambda_z = 6.0D_m$ and $a = 0.25D_m$ with an improvement of 70%. This superiority also exists in a wider range of reduced velocities, leading to a power increase of 121%. The behavior of the oscillation echoes the observations made on the energy. The flow field results reveal that at $\lambda_z = 6.0D_m$ and $a = 0.25D_m$, hairpin vortexes with legs attaching on the two sides of the node are observed, producing a wide wake near the node while a narrow wake near the saddle. However, an opposite scenario is observed for the case with the worst performance, i.e., $\lambda_z = 1.8D_m$ and $a = 0.25D_m$. The former wake distribution seems to create a larger pressure difference over the wavy cylinder, induce a larger oscillation and hence improve the power output.

1. Introduction

Renewable energy from air or water flows is widely available across the Earth and thus great efforts have been made to harness this type of flow energy. Among others, flow-induced vibration (FIV) of a slender bluff body, including vortex-induced vibration (VIV), galloping and fluttering, has mostly been taken as the kinetic source of energy harvester; see the excellent compendiums by Abdelkefi[1], Hamlehdar *et al.*[2], Wang et al.[3] and Ma et al.[4].

To improve the performance of FIV-based flow-energy harvesters, various methods have been proposed to enhance the dynamic response of the bluff body, e.g., modifying the cross-section shape of a bluff-body (Kwon[5]; Yang *et al.*[6]; Liu *et al.*[7]; He *et al.*[8] ;Yang *et al.*[9] ; Zhao *et al.*[10]; Wang *et al.*[11] ; Jeon *et al.*[12]), installing fins at the corner of a square prism (Hu *et al.*[13]), attaching small rods on the windward side of a circular cylinder (Hu *et al.*[14] and Hu *et al.*[15]) or splitter plates on the leeward/windward side (Song *et al.*[16] and Wang *et al.*[17, 18]), using tandem bluff-bodes[19]. According to Kwon[5] and Liu *et al.*[7], a bluff body with a T- or Y-type cross-section can initiate fluttering at a lower wind speed and generate more energy, compared to a plain prism. Effects of the cross-section shape on the performance of a bluff body was investigated by He *et al.*[8] and Yang *et al.*[9], where a rectangular cross-section of different aspect ratios, an equilateral triangular cross-section and a D-shaped cross-section were taken into account. For a square prism, Hu *et al.*[13] added miniature fins at the leading-edge corners and noticeably boosted galloping, thus achieving substantial improvement in the efficiency of the energy harvester. Through wind tunnel tests, Hu *et al.*[14] studied the performance of a circular cylinder by symmetrically attaching two small rods about the windward stagnation point, which was inspired by rain-wind-induced vibration of stay-cables of cable-stayed bridges. They found that the aeroelastic unstable range of the circular cylinder was significantly expanded when the circumferential location of the small rods was 60°. Alternatively, a splitter plate was attached to the leeward side of a circular cylinder by Song *et al.*[16] to trigger the galloping and hence improve energy harvesting.

Wang *et al.*[17] further extended the isolate splitter plate into a Y shaped attachment on the windward side of the cylinder, with a better performance observed. Wang *et al.* [11] also tested the performance of a piezoelectric wind energy scavenger under different cross-sectioned bluff bodies at various incident angles. Up to 71% improvement on the maximum output voltage can be attained for the cross-section of combined circular- and cuboid-foams at zero incident angle. With the concept of topological equivalent aerodynamics, Zhao *et al.*[10] designed a funnel-shaped bluff body and observed improved energy harvesting at a wide range of wind velocity. A novel adaptive energy harvester, having a transformable cross-section with wind velocity, is proposed by Jeon *et al.*[12] and the maximum improvement up to 39% was obtained. Kim *et al.*[19] developed an energy harvester which included two types of D shape bluff bodies: fixed (downstream) and oscillating (upstream). Compared with isolated oscillating body, the new system even could generate 20 times more electric power.

From the above surveys, one can see that the key to improve energy harvesting through FIV of a bluff body lies in triggering or boosting VIV and/or galloping. A sinusoidal wavy circular cylinder, featured by sinusoidally varying the diameter along its spanwise direction, is perhaps one of the simplest approaches to modify the cylinder geometry. Although the wavy cylinder, when fixed, is able to reduce the fluid forces (Ahmed & Bays-Muchmore[20]; Bearman & Owen[21], Lam & Lin[22], Lam *et al.*[23], Lin et al.[24] and Bai *et al.* a&b [25, 26]), FIV may occur once it is elastically supported (Zhang *et al.*[27] and Assi *et al.*[28]). This motivates us to explore the potential of energy harvesting by FIV of a wavy cylinder. To this end, a system consisting of an elastically supported wavy cylinder and a tuned mass damper (TMD) is proposed and examined in the present work. A range of geometry parameters (i.e., wavelength and wave amplitude) and TMD mass are considered. Experimental tests are conducted, together with theoretical modeling and computational-fluid-dynamics (CFD) simulations.

2. Methodology

This section serves to introduce the problem description and provide a detailed discussion of the methodology, which includes descriptions of the experimental setup, theoretical modeling, and computational fluid dynamics (CFD) simulations. The study seeks to investigate the flow-energy harvesting performance of a system consisting of a wavy cylinder and a tuned mass damper, with theoretical modeling utilized to predict voltage output for a given excitation, while CFD analysis is undertaken to assess the resultant VIV response. More details are introduced as follows.

2.1 Experimental tests

As schematically illustrated in Fig. 1(a), the wavy cylinder can be described by its diameter $D(\mathrm{z}) = D_m - 2a\cos(2\pi z/\lambda_z)$, where D_m is the mean diameter, λ_z and a are the wavelength and wave amplitude, respectively, and z denotes the spanwise direction. A system is developed to connect this wavy cylinder with a TMD, as shown in Fig. 1(b). The coupled system is elastically supported via four air bearings and two springs, allowing the wavy cylinder to oscillate transversally in cross flow. The total mass of the cylinder and its supporting air bearings is around 9.0 kg. The TMD consisting of a mass block and a supporting steel beam (320 mm long, 25 mm wide and 0.7 mm thick) is driven by the oscillating cylinder. A piezoelectric sheet of 100 mm long, 14 mm wide and 0.35 mm thick (M8514P2, Smart Material) is mechanically attached on the base of the steel beam and electronically connected to an electrical resistance $R = 1.45\times10^7\ \Omega$. As such, voltage can be generated by the piezoelectric sheet from the deformation of the steel beam. The properties of the TMD system are shown in Table 1. Specifically, the structural damping parameter of the structure is determined through a series of free-decay tests, where the electrodes are shortcircuited and denoted by R = 0 to represent without any resistive load. In contrast, the piezoelectric coupling coefficient is determined by leaving the electrodes open-circuited. In our study, since the input impedance of the A/D converter board (NI 9220) inserted on a DAQ board (NI cDAQ 9174) is much larger than that of the piezoelectric sheet, we directly connected the electrodes of the piezoelectric sheet to the input of the DAQ board, i.e., work as open-circuited. This data processing method is similar to that utilized by [29-31].

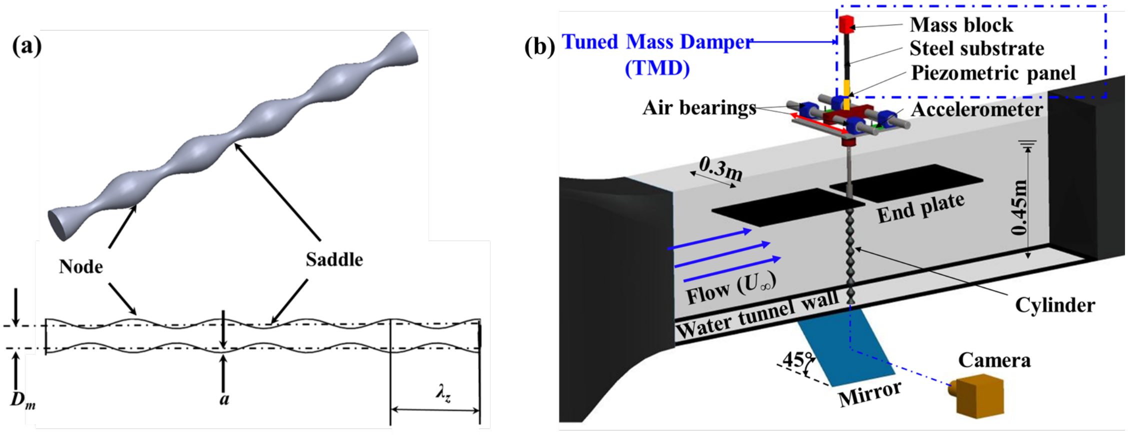

FIG.1. Experimental setup: (a) a wavy cylinder and its definition (b) the experimental arrangement in a closed-loop water tunnel.

Table 1 Properties of the TMD system

Parameter	Value
Capacitance C_p (nF)	95.8
Piezoelectric coupling coefficient θ_p (N/V)	1.51×10^{-7}
Mass density of the cantilever m_1 (kg/m^3)	7850
Young's modulus E (Gpa)	198
Damping ratio ζ	0.065

Tests are conducted in a closed-loop water tunnel, which has a test section of 0.6 m × 0.3 m × 2.2 m (depth × width × length). The wavy cylinder model, made of aluminum, has a mean diameter $D_m = 22$ mm and a length $L = 400$ mm, resulting in a blockage ratio of 7.3%. A wide range of the wavelength (λ_z) and wave amplitude (a) are considered, i.e., $\lambda_z/D_m = 1.8 \sim 6.0$ and $a/D_m = 0.152 \sim 0.25$. The gap between the cylinder bottom end and the water-tunnel bottom is around 5 mm. An end plate is placed near the top end of the cylinder to minimize the three-dimensional and free-surface effects. An accelerometer is attached on one of the air bearings to measure the transverse oscillation of the wavy cylinder. Signal from the accelerometer is sampled at 2 kHz by an A/D convertor board (NI 9220). A high-speed camera (Photron Mini UX100) operating at 250 fps was used to acquire the cylinder's motions synchronously through a mirror placed just below water tunnel at 45° with the horizontal plane for correlating the accelerometer data. Without connecting the TMD, the natural frequency of the elastically supported wavy cylinder is $f_N = 1.1$ Hz. Based on a series of free-decay tests in stationary water, the mass-damping ratio of the coupled system is $m^*\xi = 0.07$, where $m^* = 52$ is the ratio of the mass of the coupled system to the mass of water displaced by the wavy cylinder, and $\xi = 1.35 \times 10^{-3}$ is the damping ratio of the coupled system in air.

During the tests, a range of incoming velocity U_∞ is used, corresponding to a reduced velocity $U_r = U_\infty/f_N D_m = 2 \sim 14$ and a Reynolds number range $Re = \rho U_\infty D_m/\mu = 2000 \sim 8000$, where ρ and μ are the density and dynamic viscosity of water, respectively. Three mass values are adopted for the TMD, i.e., 0 g (Mass 0), 157 g (Mass 1) and 287 g (Mass 2). With these mass blocks attached, the TMD renders different natural frequencies of $f^* = f/f_N = 5.04$ (Mass 0), 1.03 (Mass 1) and 0.65 (Mass 2), as shown in Fig. 2(a). If coupled with these TMD, the frequency responses of the wavy cylinder are shown in Fig. 2(b). Clearly, when the coupled system with Mass 0 or 2 is attached, respectively, there is a large disparity in natural frequency between the TMD system and base excitation system; so, the system exhibits one significant frequency of $f^* = 1.0$, caused by the natural frequency of base excitation, i.e., air bearings - springs system. A very marginal frequency is respectively observed at $f^* = 0.65$, induced by the natural frequency of the tuned mass damper (TMD) system with its tip mass fixed at Mass 2, as shown in Fig.2(a). However, when Mass 1 is attached, the natural frequency of TMD system is very close to the elastic supported cylinder's, leading to strong coupling between two systems, and hence the coupled system shows two dominant frequencies, i.e., $f^* = 0.95$ and 1.1. The detail explanation about this bimodal phenomenon can refer to [32].

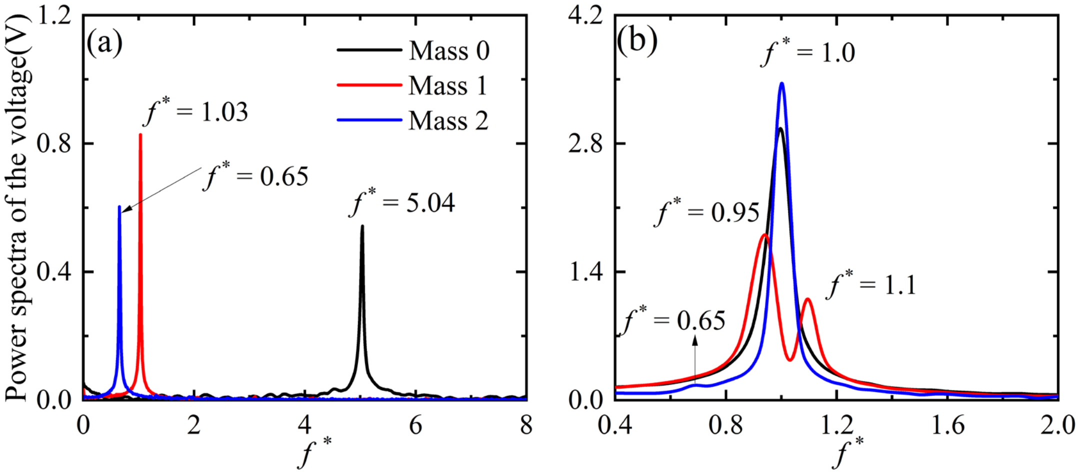

FIG.2. Experimental results of the frequency responses of (a) the tuned mass damper (TMD) system including the mass block and the steel substrate, and (b) the coupled system. Three different masses (i.e., Mass 0, 1 and 2) are considered

2.2 Theoretical Modeling

In this section, a simplified model is developed to describe the electromechanical dynamics of the coupled system. Fig.3 displays a simplified schematic of the energy harvesting system, including a piezoelectric sheet, cantilever beam and mass block. The bottom end of the beam is connected with the air bearing system and cylinders. In order to avoid the slip between piezoelectric sheet and beam, a piezoelectric sheet is tightly glued to cantilever beam from the left end of beam. With the incoming flow, the bottom end of the beam oscillates along with the air bearing. Due to motion difference between the tip Mass and bottom end of the beam, the piezoelectric patch deforms together with beam and generates power.

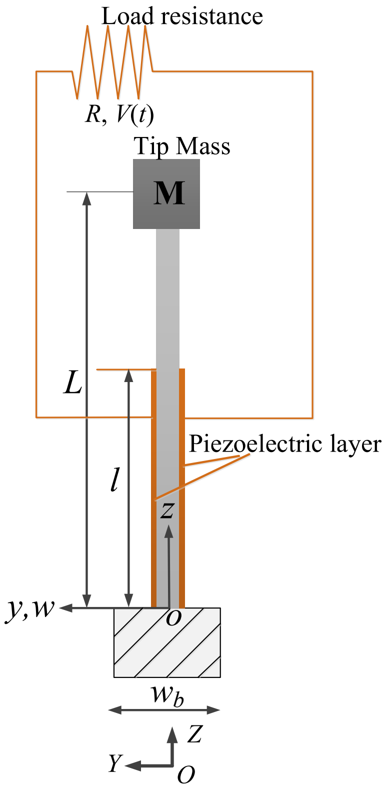

FIG. 3. Schematic of the simplified experimental energy harvesting system

The coupled mechanical and electrical equations of the piezoelectric cantilever subjected to the base excitation can be expressed as follows with only keeping the fundamental mode[30, 33, 34], and its detailed derivation can be found in Appendix A.

$$\ddot{\eta}(t) + 2\zeta\omega\dot{\eta}(t) + \omega^2\eta(t) + \theta_p V(t) = f(t) \tag{1}$$

$$\frac{V(t)}{R} - \theta_p\dot{\eta}(t) + C_p\frac{dV(t)}{dt} = 0 \tag{2}$$

where η, ζ, and ω are the modal coordinate, damping ratio, and natural frequency of the cantilever beam, respectively. θ_p is the modal electromechanical coupling coefficient, $V(t)$ is the voltage across the piezoelectric layers and $f(t)$ represents the forcing function due to base excitation. In the circuit Eq. (2), R is the simple resistive load and C_p is the capacitance of the piezoelectric transducer.

Motivated by [33, 35, 36], the translation of the base displacement is given with the form $w_b(\mathrm{t})=A_b e^{\mathrm{i}\Omega \mathrm{t}}$, where A_b is the translational displacement amplitude of the base, Ω is the frequency and i is the unit imaginary number, then the steady-state model mechanical and voltage response across the resistive can be assumed to be harmonic at the same frequency as $\eta(\mathrm{t})=A_m e^{i\Omega t}$ and $V(\mathrm{t})=V_m e^{i\Omega t}$, where A_m and V_m are the amplitudes of mode coordinate and output voltage, respectively. By substituting them into the electrical Eq. (2), the relationship between the maximum voltage output and the amplitudes of the mode coordinate is obtained as

$$V_{max} = \frac{R\theta_p\Omega}{\sqrt{C_P^2R^2\Omega^2+1}}|A_m| \tag{3}$$

By rebuilding the coupling term $\theta_p V(t)$ as a function of $\eta(t)$ and $\dot{\eta}(t)$, the mechanical governing equation for the piezoelectric cantilever is expressed as:

$$\ddot{\eta}(t) + \left[2\zeta\omega + \frac{R\theta_P^2}{C_P^2R^2\Omega^2+1}\right]\dot{\eta}(t) + [\omega^2 + \frac{C_PR^2\Omega^2\theta_P^2}{C_P^2R^2\Omega^2+1}]\eta(t) = f(t) \tag{4}$$

So, the modified frequency and damping ratio are written as

$$\bar{\omega} = \sqrt{\left[\omega^2 + \frac{C_PR^2\Omega^2\theta_P^2}{C_P^2R^2\Omega^2+1}\right]} \qquad \bar{\zeta} = \frac{2\zeta\omega+\frac{R\theta_P^2}{C_P^2R^2\Omega^2+1}}{2\bar{\omega}} \tag{5}$$

Considering the force source f as $(m\int_0^L \phi\,(z)dz + M\phi(L))A_b\Omega^2e^{\mathrm{i}\Omega\mathrm{t}}$, where $\phi(z)$ is the fundamental eigenfunction of the cantilever beam, the mode coordinate of the beam can be solved by Eq. (4) and described as:

$$A_m = \frac{m\int_0^L \phi(z)dz+M\phi(L)}{\sqrt{\left[\left(\frac{\bar{\omega}}{\Omega}\right)^2-1\right]^2+\left[\left[2\bar{\zeta}\left(\frac{\bar{\omega}}{\Omega}\right)\right]\right]^2}}A_b \tag{6}$$

Thus, the relationship between the amplitudes of output voltage and displacement is given

$$V_m = \frac{R\theta_p\Omega}{\sqrt{\Omega^2C_P^2R^2+1}}\left|\frac{m\int_0^L \phi(z)dz+M\phi(L)}{\sqrt{\left[\left(\frac{\bar{\omega}}{\Omega}\right)^2-1\right]^2+\left[2\bar{\zeta}\left(\frac{\bar{\omega}}{\Omega}\right)\right]^2}}A_b\right| \tag{7}$$

Given the experimentally obtained transversal oscillation amplitude of the base, Eq. (7) provides a direct prediction of the output voltage amplitudes in the corresponding scenario. This analytical approach demonstrates the potential to predict the energy-harvesting performance of the system based on the measured parameters, offering a valuable tool for the optimization of similar systems in practical applications.

2.3 CFD simulations

The computational fluid dynamics (CFD) simulations are conducted using ANSYS Fluent. In the simulation, the computational domain is rectangular with length $L = 40D_m$ (freestream direction), width $W = 13.6D_m$ (perpendicular direction of the flow) and height $H = 3.6D_m$ (for smooth cylinder) or one wavelength (for wavy cylinder). The cylinder is located at $10D_m$ downstream from the velocity inlet and $30D_m$ upstream from the pressure outlet. The domain includes two Zone: Moving circular zone, i.e., $d = 1.5D_m$, which moves with the cylinder with the first layer $y^+ \leqslant 1$, and Deforming zone where the mesh density is decreasing with the distance between the cylinder and mesh center. In spanwise direction, periodic boundaries are applied on the top and bottom surface of domain. No-slip boundary condition is imposed on the surface of the cylinder. The dynamic response of the cylinder is seen as a single-DOF mass-spring-damper oscillator and expressed as (Khalak & Williamson[37]):

$$m\ddot{y} + c\dot{y} + ky = F_y \tag{8}$$

where the equivalent mass m, damping c and spring stiffness k of experiment are applied in the simulation. y and F_y are the oscillation displacement and vertical hydrodynamic (lift) force, respectively. To solve Eq.(8), a user defined function (UDF) is embedded into the software where the Newmark-β method is implemented for time integration (Teixeira & Awruch[38], Zhang et al.[39], Han et al.[40] and Wang & Zhao [41]). The hydromancy force F_y is simulated by solving unsteady Reynolds averaged-Navier-Stokes (RANS) equations:

$$\frac{\partial \bar{u}_i}{\partial x_i} = 0 \tag{9}$$

$$\frac{\partial \rho \bar{u}_i}{\partial t} + \frac{\partial \rho \overline{u_i u_j}}{\partial x_i} = -\frac{\partial \bar{p}}{\partial x_i} + \mu \nabla^2 \bar{u}_i - \frac{\partial \rho \overline{u_i' u_j'}}{\partial x_j} \tag{10}$$

where u is the velocity, p the pressure, μ the dynamic viscosity. Subscript i and j are to indicate the directions of the components in the Cartesian coordinate system (i, j = 1, 2 or 3 for x, y, or z direction, respectively). The turbulence is modeled by the SST k-ω turbulence model. The dynamic mesh method is adopted to achieve the mesh information updating [42]. The second order upwind scheme and the first-order implicit scheme are adopted to discretize the spatial term and temporal term, respectively. The detailed validations of the simulation are shown in the Appendix B.

3. Results and discussion

3.1 Energy extraction performance

Fig. 4 shows variations of the output voltage (V_{rms}, root-mean-square value) generated by the coupled system against the reduced velocity (U_r). Comparison is made to the baseline case, i.e., the smooth cylinder (denoted as CY). Note that the output voltage from the coupled system is nearly zero when no mass (Mass 0) is added to the TMD; so, only results from the coupled system with Mass 1 (Fig. 4a) or Mass 2 (Fig. 4b) are presented. In general, the output voltage V_{rms} from the coupled system is noticeably enhanced in a range of the reduced velocity U_r, regardless of the cylinder type and associated configurations (including wavelength and wave amplitude of the wavy cylinder, and mass added to the TMD). This is ascribed to flow-induced vibration (FIV) of the smooth or wavy cylinder that is driven by alternating lateral lift forces and, simultaneously, the FIV of the cylinder could render deformation of the steel beam to generate piezoelectric voltage.

Specifically, for the coupled system of the smooth cylinder and the TMD with Mass 1 (Fig. 4a), the output voltage V_{rms} is larger than zero in the FIV range of $4.0 < U_r < 9.0$, with the maximum $V_{rms} = 1.28$ volt reached at $U_r = 5.3$. Outside of the FIV range, $V_{rms} \approx 0$. In terms of the coupled system of the wavy cylinder and the TMD with Mass 1, a strong dependence of the output voltage on the cylinder configuration can be observed in Fig. 4(a). When the wavy cylinder has the shortest wavelength $\lambda_z/D_m = 1.8$ tested in this work (see Fig. 4a1), the output voltage is lower than that from the baseline case in the VIV range when $U_r > 5.0$. This suggests that FIV of the wavy cylinder with $\lambda_z/D_m = 1.8$ is suppressed, compared to that of the smooth cylinder (A detail discussion related the dynamic responses of cylinders is introduced in Sec. 3.2). When the wavelength of the wavy cylinder is increased to $\lambda_z/D_m \geq 3.6$ (Fig. 4 a2 & a3), the output voltage V_{rms} exhibits different behavior from the case with the shortest wavelength. Firstly, with the increase of wavelength at a given wave amplitude, the non-zero output voltage V_{rms} range is increased and shifted towards higher reduced velocities, particularly for the largest wavelength $\lambda_z/D_m = 6.0$ tested in this work. Secondly, the output voltage V_{rms} is significantly enhanced for the coupled system of the wavy cylinder with $\lambda_z/D_m = 6.0$ and $a/D_m = 0.25$. Around $U_r = 7.3$, its maximum output voltage $V_{rms} = 1.6$ volt is attained, which is 25% higher than that of the baseline case. In Fig. 4(b), where the coupled system includes the largest Mass 2, similar patterns can be observed. However, the magnitude of the output voltage in Fig. 4(b) is overall lower than that in Fig. 4(a).

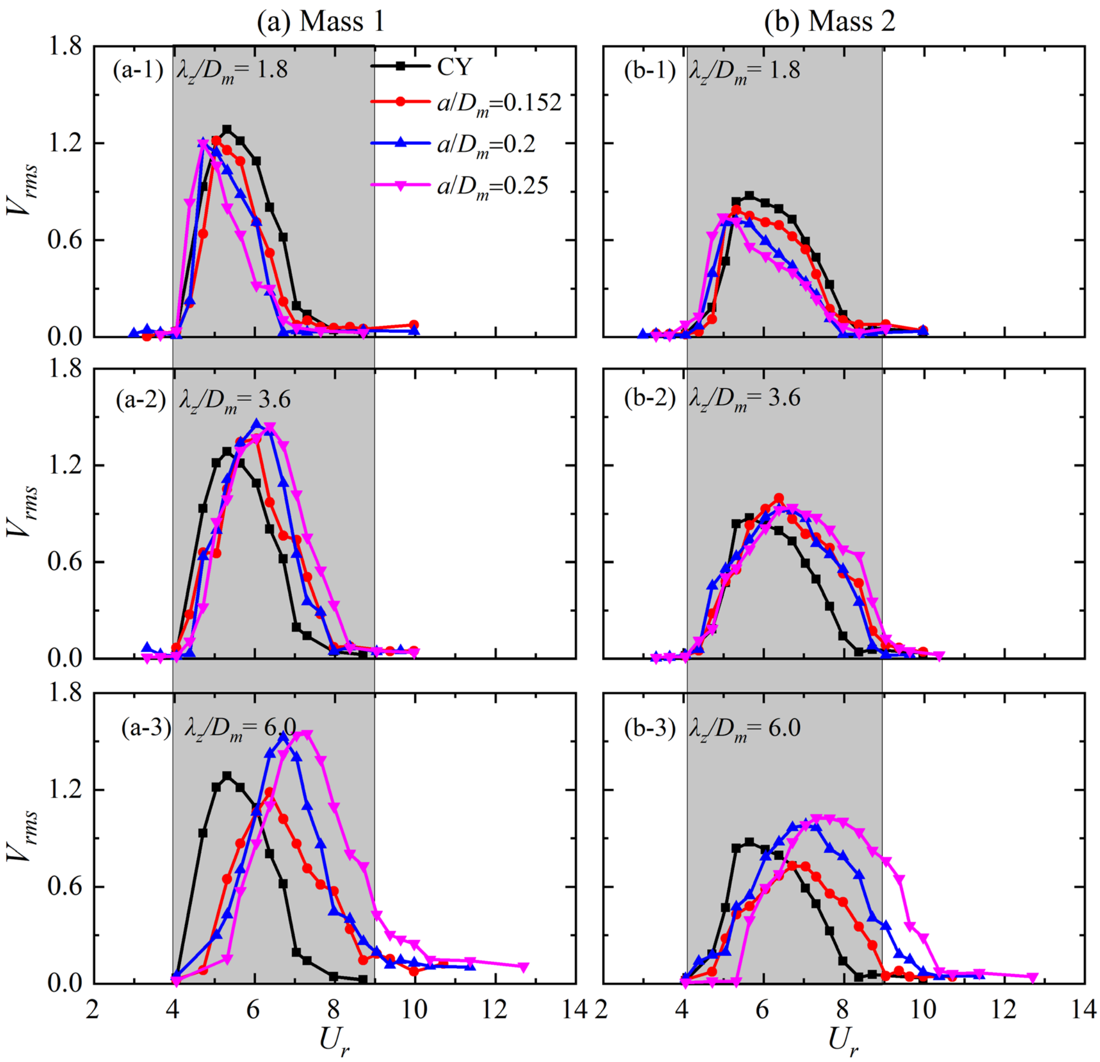

FIG. 4. Experimental results of the variations with reduced velocity (U_r) in the output voltage (V_{rms}) of the coupled system, the wavy cylinders being with different wave lengths (a1, b1: λ_z=1.8D_m; a2, b2: 3.6D_m; a3, b3: 6.0D_m). Mass 1 (a) or Mass 2 (b) is added in the coupled system. The shaded area indicates the range of reduced velocity where flow-induced vibration of the baseline case (i.e., a smooth cylinder) occurs.

Fig. 5 further exhibits the variations of the frequency of output voltage (f_V/f_N) with the reduced velocities U_r. In Fig. 5(a), where Mass 1 is added to the TMD system, the TMD system starts locking in a lower frequency, around f_V/f_N = 0.96. However, with U_r reaching enough large values, it jumps to f_V/f_N = 1.15. So, two dominant lock-in frequencies are observed over the whole U_r range. When Mass 2 is applied to the TMD system, the dominant lock-in frequency of the output voltage increases very mildly with the incoming velocity, leading to one dominant frequency closed to 1.0 regardless of cylinder types and reduced velocities (see Fig. 5b).

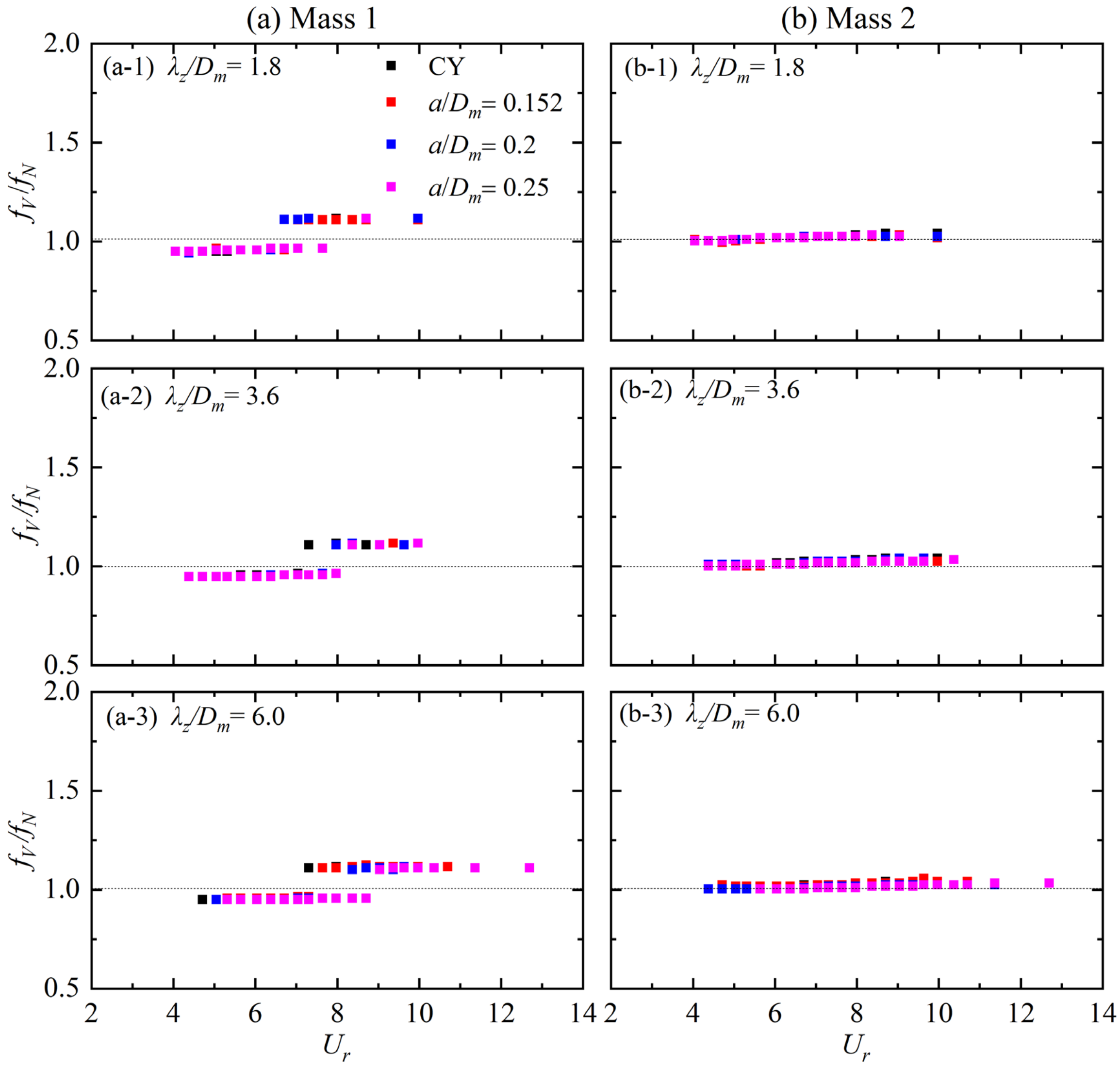

FIG.5. Experimental results of the variations with reduced velocity (U_r) in the output voltage frequency (f_V/f_N) for the wavy cylinders being with different wave lengths (a1, b1: λ_z=1.8D_m; a2, b2: 3.6D_m; a3, b3: 6.0D_m). Mass 1 (a) and Mass 2 (b) are added in the coupled system, respectively.

Based on the power output (i.e., $P = V_{rms}^2/R$) from the coupled system where Mass 1 or Mass 2 is added to the TMD, respectively, further discussion is made on energy harvesting performance of the worst case (λ_z/D_m = 1.8 and a/D_m = 0.25), the best case (λ_z/D_m = 6.0 and a/D_m = 0.25) and the baseline case (smooth cylinder). Fig. 6(a) displays the variations of P with U_r, while Fig. 6(b) shows the integrated power output over the U_r range for the coupled systems of different cylinders and masses. As indicated in Fig.6(a). the maximum power output from the coupled system of the smooth cylinder reaches P_{max} = 11.4 × 10^{-2} μW at U_r = 5.3 when Mass 1 is added to the TMD system. As the wavy cylinder with λ_z/D_m = 6.0 and a/D_m = 0.25 is installed, the maximum output power from the coupled system can attain to P = 19.4 × 10^{-2} μW at U_r = 7.3. That is, the maximum power output is significantly improved by around 170%

when the smooth cylinder is replaced by the wavy cylinder with $\lambda_z/D_m = 6$ and $a/D_m = 0.25$. In Fig. 6(b), it can be observed that with U_r increasing to around $U_r = 7.3$, the integrated power output has already reached the total power of smooth cylinder generated from the entire VIV range. As for the total power in the entire VIV range, it even can be up to 41.3×10^{-2} μW for the coupled system of the wavy cylinder with $\lambda_z/D_m = 6.0$ and $a/D_m = 0.25$, which is 2.21 times that (18.7×10^{-2} μW) for the coupled system of the smooth cylinder**.** On the contrary, the maximum output power performance of the worst case (only around 9.9×10^{-2} μW) is observed at the shortest wavelength and largest amplitude, i.e., $\lambda_z/D_m = 1.8$ and $a/D_m = 0.25$ case and its total output power of the entire VIV range is only 53% of that produced by smooth cylinder. When Mass 2 is added to the TMD, the coupled system of the wavy cylinder with longest wavelength and largest wave amplitude still generates more output power in a wider FIV range than the coupled system of the smooth cylinder. Furthermore, the total output power from the former system is also larger than that from the latter system. The shortest wavelength and largest wave amplitude cylinder exhibit the opposite conclusion compared with the smooth cylinder. These observations indicate that the wavy cylinder with the longest wavelength ($\lambda_z/D_m = 6.0$) and the largest wave amplitude ($a/D_m = 0.25$) can enhance the FIV-based energy harvesting, with significantly more energy utilized from the coupled system of the wavy cylinder and the TMD, compared to that of the smooth cylinder. Nevertheless, the cylinder with the shortest wavelength ($\lambda_z/D_m = 1.8$) and largest amplitude ($a/D_m = 0.25$) can suppress system performance.

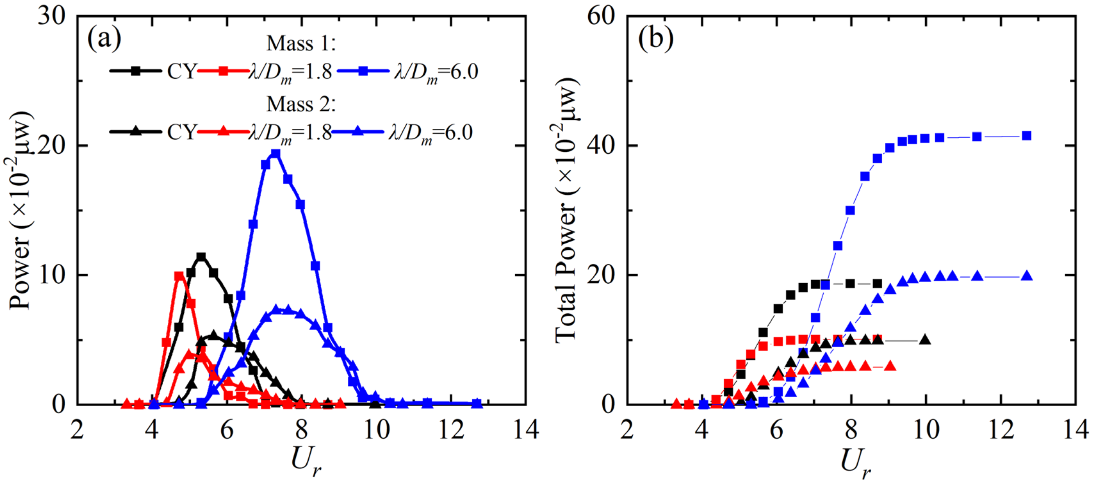

FIG. 6. Experimental results of the variations with reduced velocity in (a) the output power of the coupled system (wavy cylinder: $\lambda_z = 1.8, 6.0D_m$ and $a = 0.25D_m$) and (b) the total output power of the coupled system with the wavy cylinder (λ_z=1.8, 6.0D_m and a=0.25D_m), with Mass 1 or Mass 2 added.

3.2 Dynamic response of the wavy cylinder

Since the energy-harvesting performance of the TMD system is induced by the motions of cylinders, analyzing the dynamics of cylinders can help better understand energy harvesting performance revealed in Section 3.1. Both the best (λ_z/D_m = 6.0) and the worst (λ_z/D_m = 1.8) energy extraction performance are observed with the largest wave amplitude, i.e., $a/D_m = 0.25$. Hence, in the following sections, the wave amplitude is fixed at a/D_m = 0.25 and only wavy cylinders with various wave lengths are discussed.

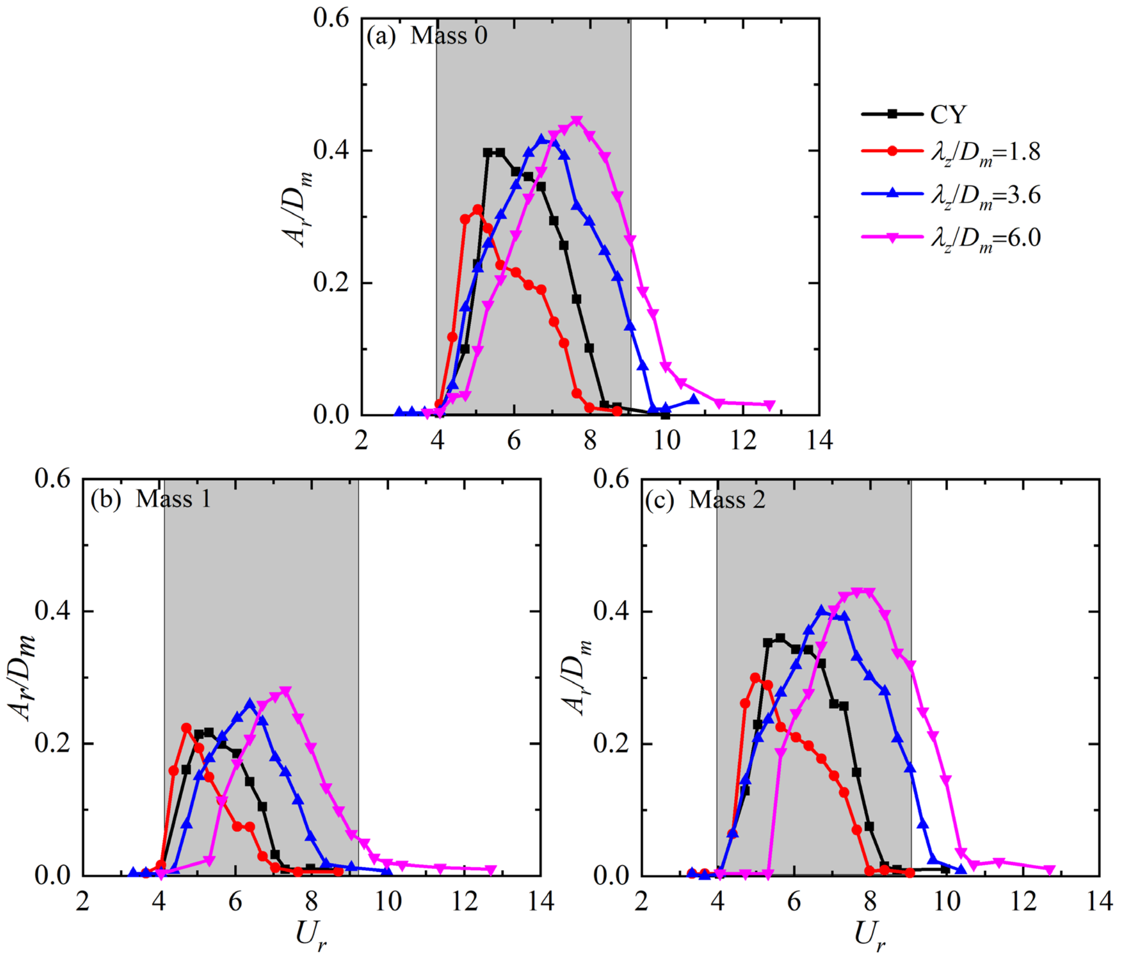

FIG.7. Experimental results of the variations with reduced velocity (U_r) in the transversal oscillation displacement (A_r) for the wavy cylinder with different wave lengths (λ_z = 1.8, 3.6 and 6.0D_m) and a fixed wave amplitude a = 0.25D_m; Mass 0 (a), Mass 1 (b), and Mass 2 (c) are added in the coupled system, respectively.

Fig. 7 shows variations with the reduced velocity (U_r) in the transversal displacement (A_r/D_m) of the wavy cylinder, considering three different wavelengths (λ_z/D_m = 1.8, 3.6 and 6.0). When the wavy cylinder of the shortest λ_z/D_m = 1.8 is installed in the coupled system, the transversal displacement (A_r/D_m) of the wavy cylinder is reduced (Fig. 7 a & c) or almost unchanged (Fig. 7b) in the maximum magnitude, depending on the tip Mass added to the TMD, compared to the baseline case. However, once the wavelength of the wavy cylinder increased to $\lambda_z/D_m \geq 3.6$, the transversal displacement A_z/D_m increased, and the VIV range seems to shift towards higher value of U_r. These observations are consistent with those seen on the output voltage or power from the coupled system. Additionally, due to the resonance between elastic supported cylinders and TMD system, the system with Mass 1 is always exhibiting the smallest transverse displacement (Ar/Dm) among the different tip Mass conditions.

In addition to the transverse oscillation displacement, the transverse oscillation frequency (f_y/f_N) also influences the system performance significantly. Hence, Fig. 8 displays the variations of the oscillation frequency of the wavy cylinder with three different wavelengths (λ_z/D_m = 1.8, 3.6 and 6) compared with the smooth cylinder at various reduced velocities. Just like in Fig. 5, all the cases' frequencies are very close to 1 (f_y/f_N = 0.95-1.1) in the lock-in region. This means that although the wavy surface of cylinder can modify its relevant VIV zone range and even oscillation amplitudes, the dynamics of cylinders is still VIV. Specially, as Mass 0 and Mass 2 are added in the coupling system, respectively, the lock-in frequency of the coupling system increases smoothly with reduced velocity (see Fig.8 a & c); however, with the Mass 1 applied, there are two dominant frequencies, i.e., f_y/f_N = 0.98 and 1.1 (see Fig. 8b).

To further elaborate frequency distribution with various Mass added, Fig. 9 plots the frequency responses of the transversal oscillation displacement (A_r) for different cylinders. As shown in Fig. 9 (a1) to (d1), where the maximum oscillation amplitude occurs, the coupling system with Mass 1 also shows one dominant lock-in frequency f_y/f_N = 0.95 which is slightly less than that observed in the system of Mass 0 and Mass 2. With the incoming velocity increased, the second peak appears in the case with Mass 1, as indicated in Fig. 9 (a2) to (d2). As the flow velocity further increases, the second peak of frequency could even develop into the dominant one, as revealed in Fig. 9 (a3), (b3) and (d3). Actually, these frequency differences associate with the natural frequency distribution of TMD system in Fig. 2. At lower flow velocity, the frequency of the driven motion produced by various cylinders is closed to 0.95; so, the coupling system with Mass 1 traps to the first peak of natural frequency f_y/f_N = 0.95 in Fig. 2(b). With the reduced velocity increased, the frequency of the driven motion also increases, gradually approaching the second peak f_y/f_N = 1.1 and thus enforces TMD system to lock into a higher frequency f_y/f_N = 1.1. Since only one natural frequency exists in the coupling system with Mass 2 in Fig. 2 (b), it is not surprising to see only one dominant frequency over the entire range of excitation frequencies in Fig. 9 (a) and (c).

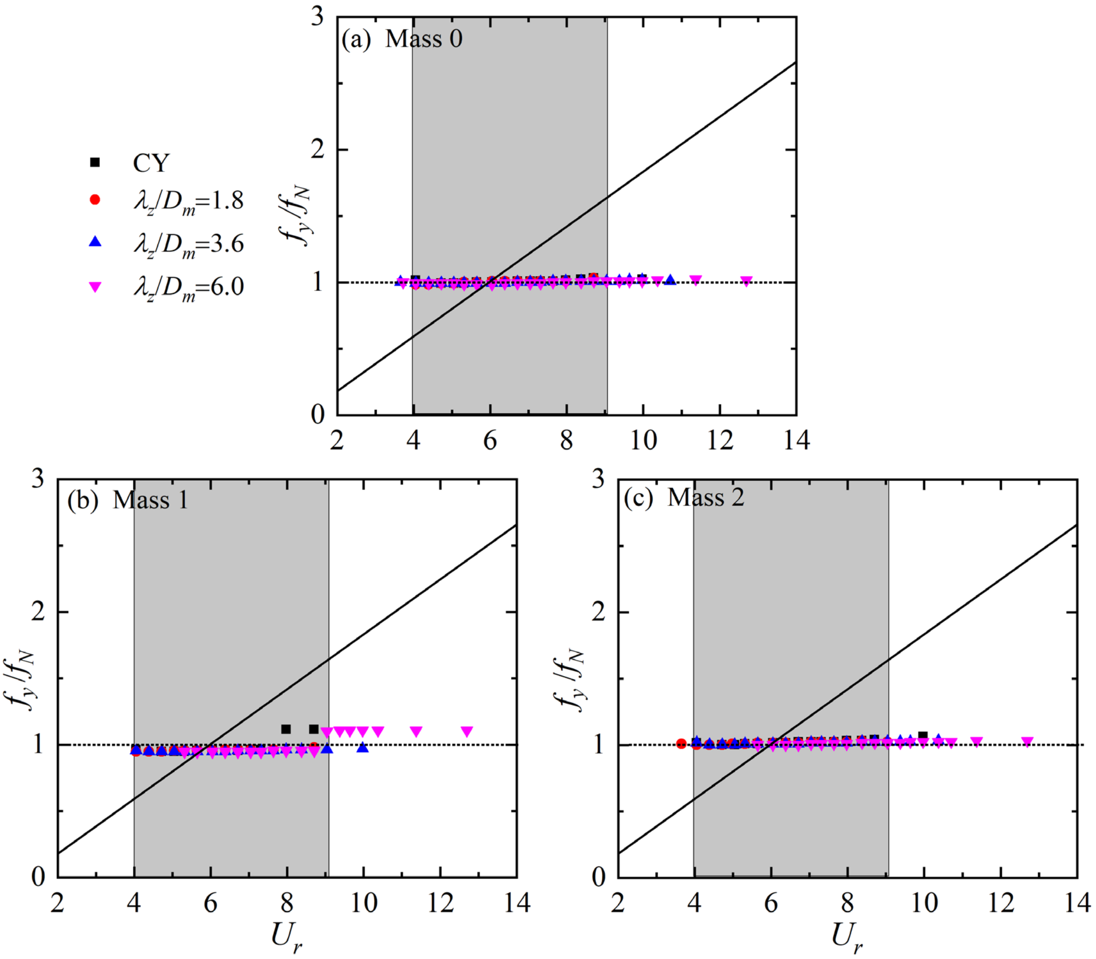

FIG.8. Experimental results of the variations with reduced velocity (U_r) in the transversal oscillation frequency (f_y/f_N) for the wavy cylinder with different wave lengths (λ_z = 1.8, 3.6 and 6.0D_m) and a fixed wave amplitude a = 0.25D_m; Mass 0 (a), Mass 1 (b), and Mass 2 (b) are added in the coupled system, respectively.

The transverse oscillation amplitude of the base, Ab, obtained experimentally, serves as the input parameter for the theoretical model presented in this study. By applying Eq.(7), the model provides a direct prediction of the output voltage amplitudes in the given scenario. Fig. 10 plots the variations of the experimental data and the theoretical predictions of the output voltage ($V_m \approx \sqrt{2}V_r$) in the oscillation displacement ($A_b \approx \sqrt{2}A_r$) for various cases with wave amplitude a = 0.25D_m. It can be found that a good agreement is achieved between the experimental and theoretical predicted results, especially when large vibration occurs. A linear relationship can be observed between the output voltage and the oscillation displacement. Moreover, a different slope can be seen at the system with various Masses attached (Mass 1: V_{rms} = 5.8*A_r/D and Mass 2: V_{rms} = 2.4*A_r/D). It means that the coupling system with Mass 1 added can generate more energy than that with Mass 2 at a same oscillation amplitude. The reason is that, in this system, the excitation (FIV) frequencies are always closed to the natural frequency system, i.e., $f_y/f_N \approx 1$ when the significant vibration happens (see Fig.8). As Mass 1 is applied in the TMD system, the resonance between base excitation generated by the oscillation of cylinders and TMD system can be achieved, i.e., $\left(\frac{\bar{\omega}}{\Omega}\right)^2 - 1 \approx 0$ in Eq. (7). Consequently, more energy can be harvested by the system with Mass 1 in comparison with that of Mass 2.

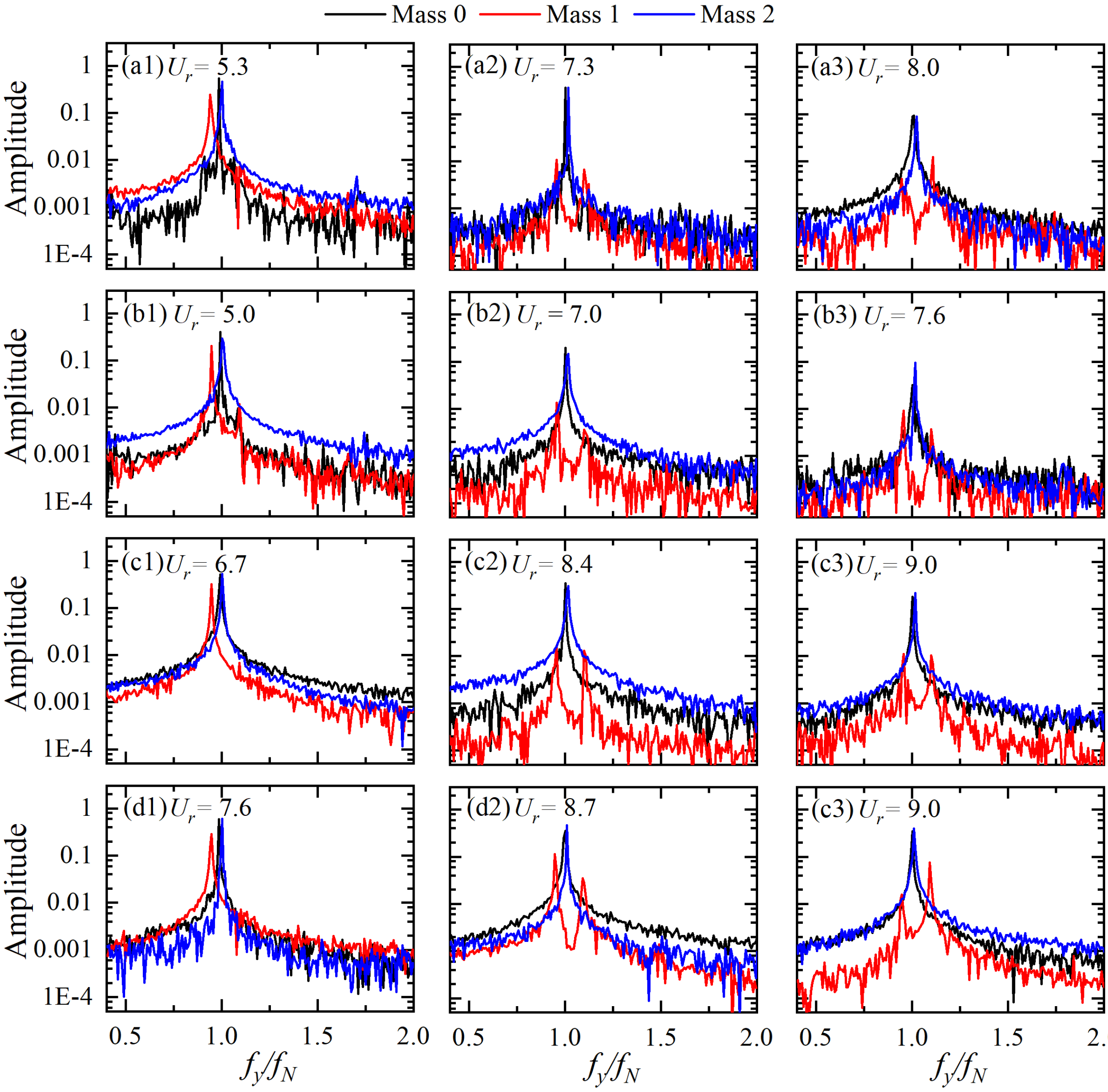

FIG.9. Experimental results of the frequency responses of the transversal oscillation displacement (A_r) for the different cylinders (a) smooth cylinder, (b) λ_z = 1.8, (c) 3.6 and (d) 6.0D_m with a fixed wave amplitude a = 0.25D_m.

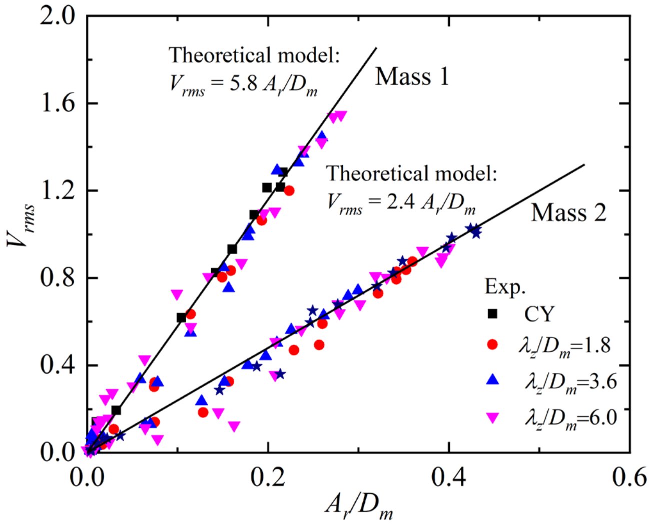

FIG.10. Variations of the output voltage (V_{rms}) in the transversal oscillation displacement (A_r/D_m) for the wavy cylinder with different wave lengths (λ_z = 1.8, 3.6 and 6.0D_m) and a fixed wave amplitude a = 0.25D_m; Mass 1 and Mass 2 are added in the coupled system, respectively. The symbols are measured by experiments and the black lines are calculated by theoretical model.

3.3 Vortex formation and flow structures

To uncover the reason why wavy cylinder with λ_z/D_m = 1.8 and 6.0 at wave amplitude a/D_m = 0.25 exhibit the worst and best, respectively. CFD simulations are conducted to reveal flow details around the cylinders. Since the oscillation displacement variation trend does not rely on the tip mass of TMD with the free stream velocity (Ur) in Fig.7, to simplify the analysis, we are only the focused on the cases with Mass 0 attached, suggesting no output voltage from the TMD system, in this section. In Fig. 7, the smooth cylinder and wavy cylinders with λ_z/D_m = 1.8, λ_z/D_m = 6.0 achieve their peak displacement around U_r = 5.3, 5.0 and 7.6, respectively. Thus, simulations are also conducted at these velocities.

The Q criterion is used to identify the three dimensional vortices around the cylinders [43]. Fig.11 shows the iso-surface of Q = 1 superimposed by the contours of the non-dimensional axial vorticity $\omega_z^* = \left(\frac{\partial v}{\partial x} - \frac{\partial u}{\partial y}\right) D_m / U_\infty$ at two instants corresponding to the cylinder at positive maximum position, i.e., $y/D_m = A_{max}$ and the equilibrium position i.e., y/D_m = 0, respectively. Moreover, contours of instantaneous axial vorticities ω_z^* and pressure in the node and saddle planes are presented in Fig. 12. For the near wake of smooth cylinder, the vortices are well organized, showing obvious 2D feature (see Fig. 11a). The Kármán vortex street is evident in Fig.12 (a). Specially, when the shear layer detaches from the smooth cylinder, it rolls up into a vortex and creates a low-pressure region near the lower surface of cylinder. As such, a net vertical hydrodynamic force is generated to drive the cylinder to move from the top extreme

(Fig.12a1) towards the equilibrium position (Fig.12a2). When the cylinder further moves away from the equilibrium position, an opposite force is produced to force the cylinder slow down till to the bottom extreme.

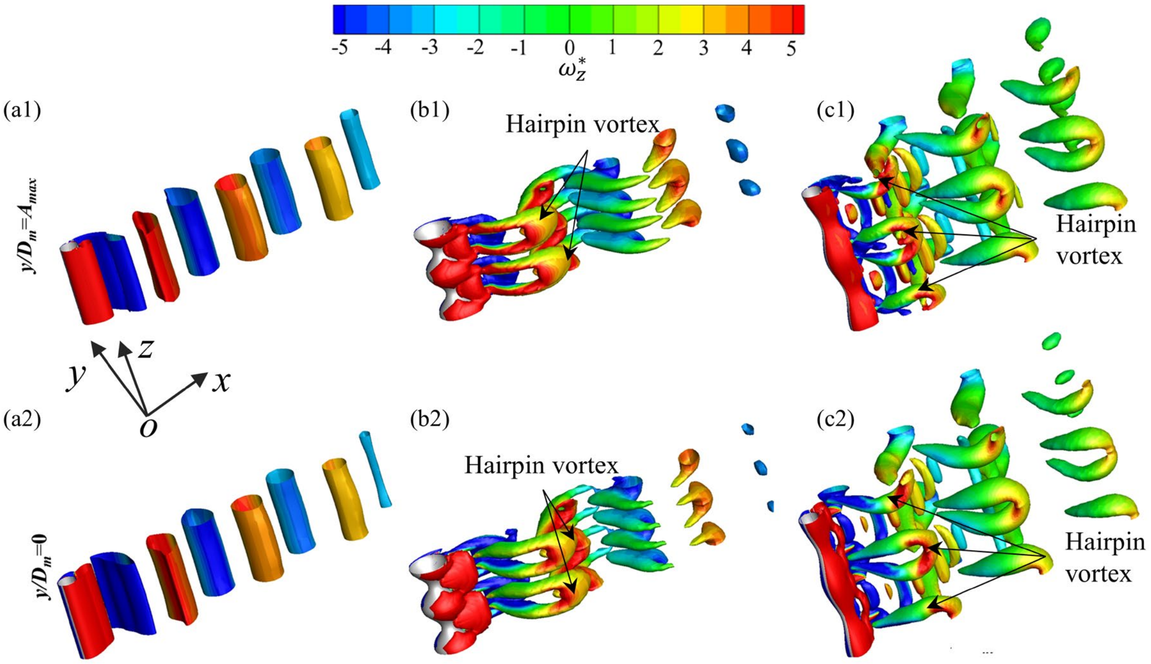

FIG.11. CFD results of the near wake structures, in terms of iso-surface of $Q = 1$ colored by ω_z^*, for the (a) smooth cylinder at $U_r = 5.3$, (b) wavy cylinder with $\lambda_z/D_m = 1.8$ at $U_r = 5.0$, and (c) wavy cylinder with $\lambda_z/D_m = 6.0$ at $U_r = 7.6$ where the wave amplitude is fixed at $a = 0.25D_m$. '1' and '2' in each column correspond to the location of the oscillating cylinder at $y/D_m = A_{max}$ and $y/D_m = 0$.

For the wavy cylinder with λ_z/D_m =1.8, its near wake is significantly three-dimensional after the shear layer separates from wavy cylinder, as shown in Fig. 11(b). Classical hairpin vortexes with legs attaching on sides of nodes appear in the near wake of elastic supported wavy cylinder, as indicated in Fig. 11(b). Due to the counter-rotating flow of hairpin vortex legs, a spanwise flow from the saddle to the node is created, producing a wider and narrower wake in the saddle plane (see Fig. 12b) and the node plane (see Fig. 12c), respectively. The strength of vorticity also seems slightly weaker than that in the smooth cylinder. Corresponding to these wake distributions, the pressure difference in both planes (especially in the node plane) is also less than that of the smooth cylinder. Since the lift force is an integration of surface area and pressure difference, i.e., $F_y = \oint P_y \, dA$, where P_y is the pressure perpendicular to the flow direction, it is not surprising to see a smaller oscillation amplitude in the λ_z/D_m = 1.8 case. Conversely, as the wavelength increases to $\lambda_z/D_m = 6.0$, due to the hairpin vortex legs attaching on the two sides of the saddle (spanwise flow moving from the nodal location towards the saddle location), the wake in the node plane is obviously wider than it in the saddle plane, as shown in Fig.12 (d) and (e). Moreover, with the shear layer splitting from the cylinder surface, some vorticities break up from one vortex into two or more vortices in the downstream (see Fig. 12 d &e). The near wake of cylinder also become more three-dimensional and stronger (see Fig. 11c). As such, a significantly larger pressure difference appears in the node plane, compared with that at the smooth cylinder. This results in a larger lift force, promoting the oscillation of the cylinder.

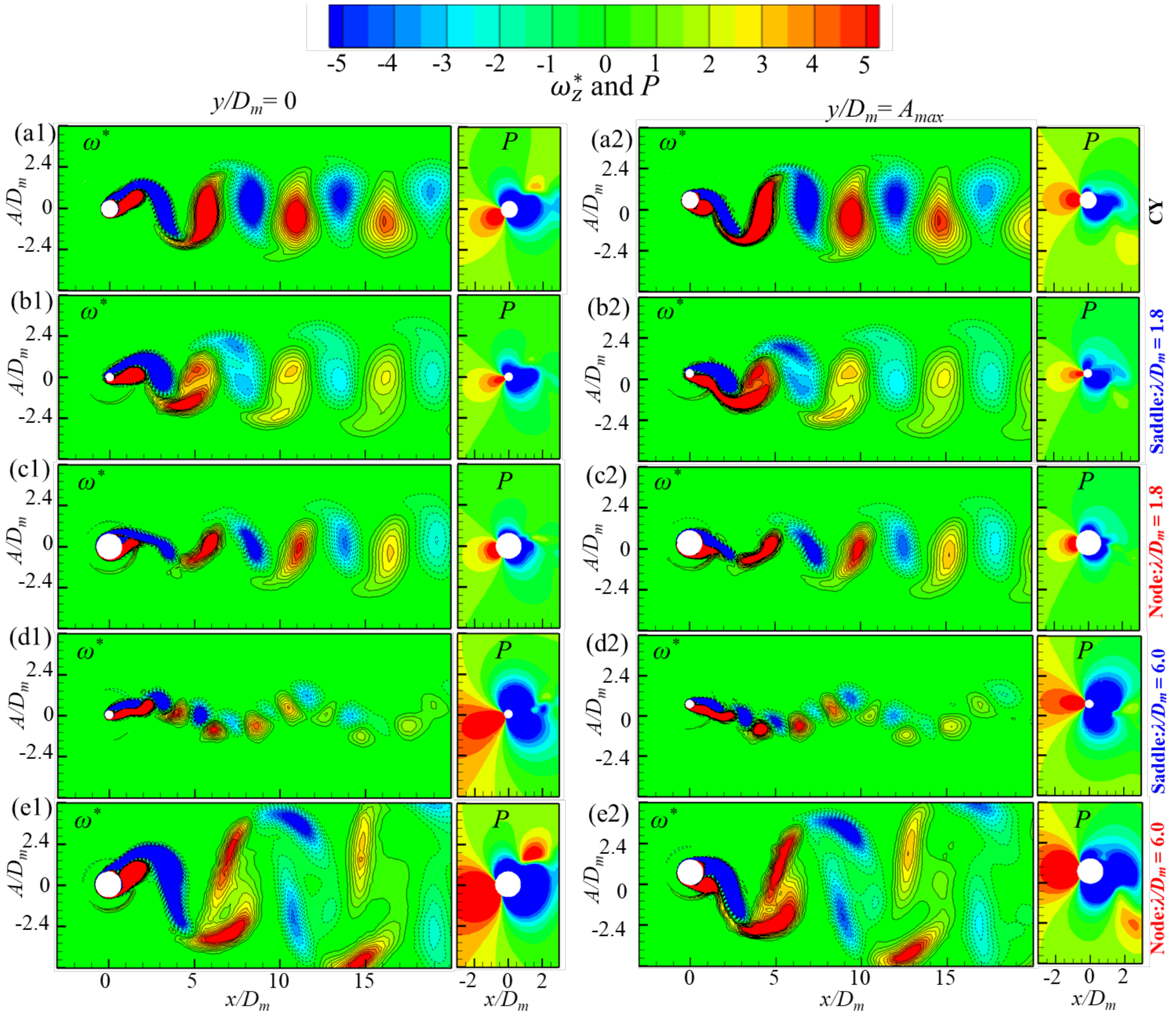

FIG.12. CFD results of contours of instantaneous vorticities ω_z^* and pressure P in different planes of the (a) smooth cylinder at $U_r = 5.3$, (b-c) wavy cylinder with $\lambda_z/D_m = 1.8$ at $U_r = 5.0$, and (d-e) wavy cylinder with $\lambda_z/D_m = 6.0$ at $U_r = 7.6$ where the wave amplitude is fixed at $a = 0.25D_m$. ‘1’ and ‘2’ in each row correspond to the location of the oscillating cylinder at $y/D_m = A_{max}$ and $y/D_m = 0$, respectively.

To offer a deeper understanding of the wake structures surrounding the cylinder surfaces, particularly for the front-shape of the wavy cylinder, Fig. 13 introduced to present the time-averaged pressure distribution and spanwise velocity on the mid-plane of various cylinder geometries. As indicated in Fig. 13 (a), for a smooth cylinder, there is no significant pressure gradient along the spanwise direction, and therefore no apparent surface flow is observed in this direction. However, the spanwise pressure gradient and corresponding surface flows are more prominent in wavy cylinders than in smooth cylinders. Specifically, for the wavy cylinder with λ_z/D_m = 1.8 and a = 0.25D_m, the node exhibits higher pressure than the saddle, resulting in a surface flow from node to saddle on the front-shape of the wavy cylinder, see Fig.13(b). This phenomenon is also observed for the front-shape of the wavy cylinder with λ_z/D_m = 6.0 and a = 0.25D_m (see Fig.13.(c)). Concerning the rear-shape of the wavy cylinder with λ_z/D_m = 1.8 and a = 0.25D_m, a higher-pressure region is found at the saddle, labeled as 'A', relative to the node, inducing the fluid flow from saddle to node. However, for a larger cylinder wavelength of λ_z/D_m = 6.0, two higher pressure regions emerge at the node, causing a flow from node to saddle. These observations are consistent with the conclusions drawn from the hairpin vortex distribution.

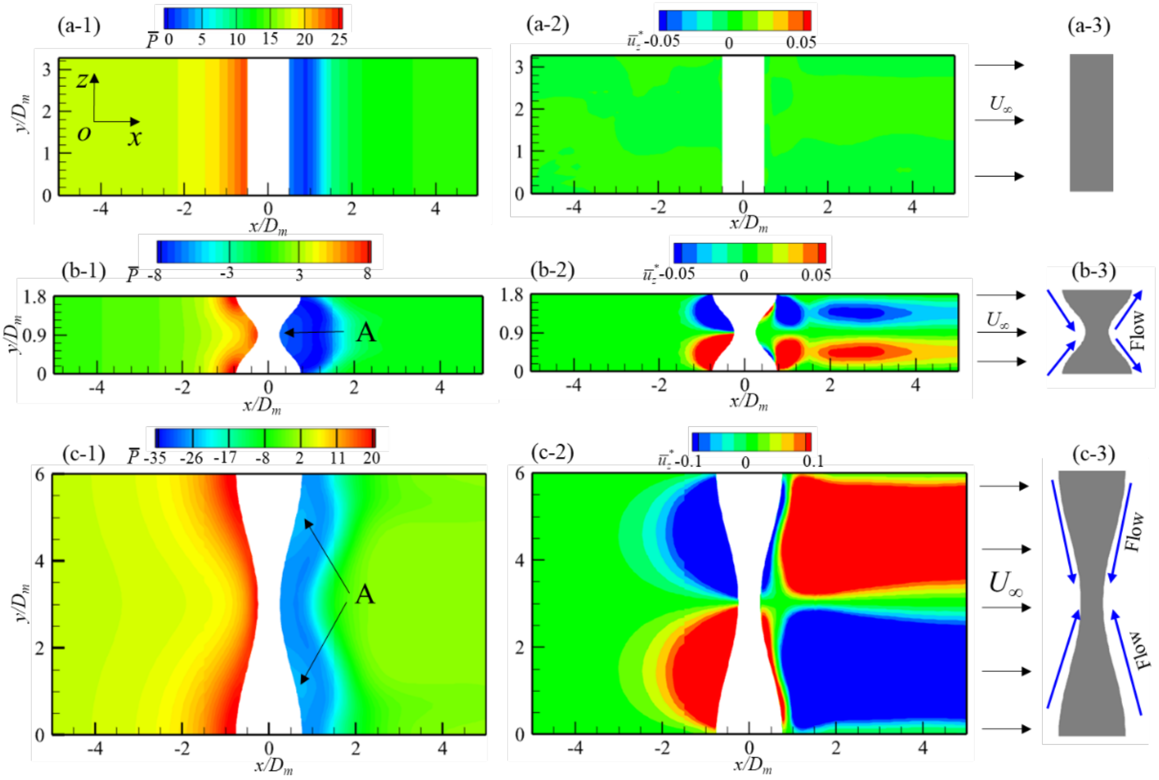

FIG.13. CFD results of contours of time-averaged pressure $\overline{P}$ and spanwise velocity $\overline{u}_z^*$ on the mid-plane planes of the (a) smooth cylinder at U_r = 5.3, (b) wavy cylinder with λ_z/D_m = 1.8 at U_r = 5.0, and (c) wavy cylinder with λ_z/D_m = 6.0 at U_r = 7.6 where the wave amplitude is fixed at a = 0.25D_m. '1' and '2' in each row correspond to time-averaged pressure $\overline{P}$ and spanwise velocity $\overline{u}_z^*$, respectively. '3' is to indicated schematics of flow direction on the surface of the flexible supported cylinder, where the blue arrow is to express the flow direction.

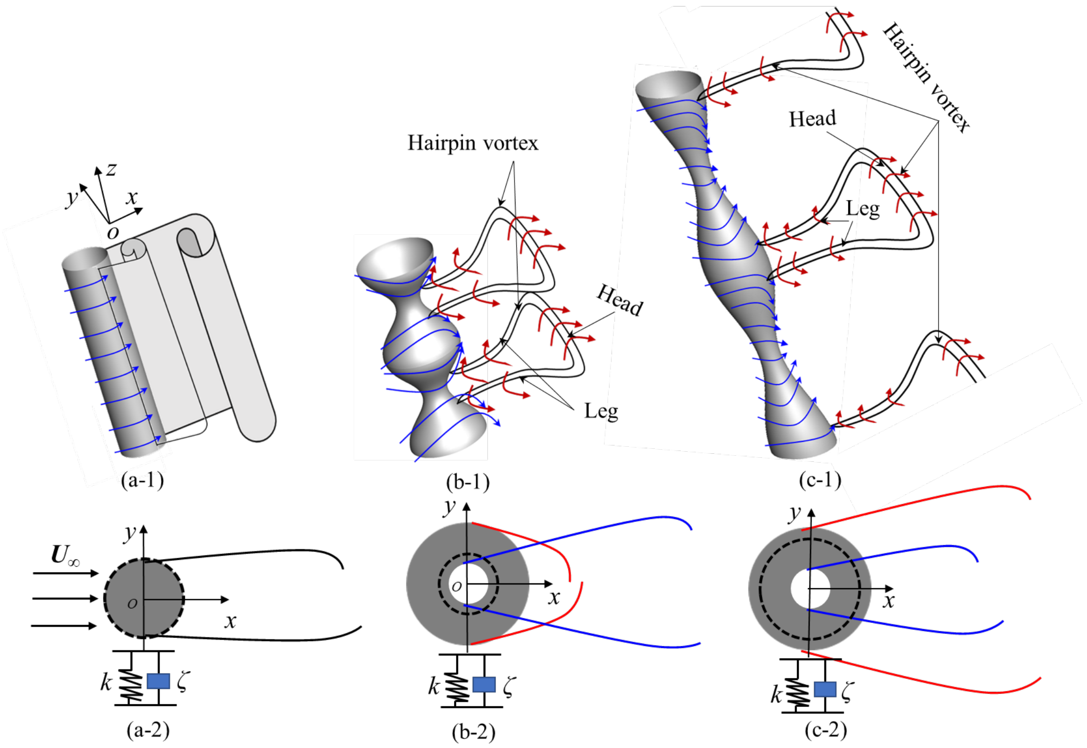

(a-1) (b-1) (c-1)

(a-2) (b-2) (c-2)

FIG.14. Schematics of wake structures around the surface of the flexible supported (a) smooth cylinder, (b) wavy cylinder with $\lambda/D_m = 1.8$ and (c) wavy cylinder with $\lambda/D_\mathrm{m} = 6.0$ where the wave amplitude is fixed at $a = 0.25D_m$. The red arrow and blue arrow are to express the flow direction of the hairpin vortex and on the surface of cylinder, respectively. The grey circular and white are to indicate the node and saddle plane, respectively. The dash line is to express the “mean diameter” d_m (estimated by the hydrodynamic force) over one wavelength. ‘1’ and ‘2’ in each column correspond to the 3D view and 2D view (top view) of the oscillating cylinder.

Based on the above CFD results and our previous studies on fixed wavy cylinder [25], Fig. 14 exhibits a sketch of wake distribution for the various elastic supported cylinders. For the smooth cylinder, 2D wake is observed (see Fig. 14a). For the wavy cylinder with $\lambda/D_m = 1.8$, the saddle exhibits a wider wake than that observed at the node plane with the effects of the spanwise flow on the surface of cylinder, as shown in Fig. 14(b). Under this wake distribution, the pressure difference at the node cross section (diameter: $D_{node} > D_m$) is obvious less than at smooth cylinder. It suggests that although the averaged geometry diameter D_m of the wavy cylinder over one wavelength is the same as the smooth cylinder, its mean diameter estimated by hydrodynamic force is less than its geometry diameter, i.e., $d_{mean} < D_m$, leading to a less oscillation amplitude and output voltage. As indicated in Fig.7, with the increase in reduced velocity, this wake distribution seems more obvious and hence causes a better oscillation suppression at higher reduced velocity. For the wavy cylinder with $\lambda/D_m = 6.0$, a significant wider wake is observed at the node plane while a narrower wake is generated at the saddle plane (evidenced in Fig. 14c). As such, a larger pressure difference occurs at the node cross section than at smooth cylinder, and further generates a larger d_{mean}. In turn, the lift force is improved, enhancing the oscillation of cylinder. Since the wavy cylinder's lock-in range shifts into larger reduced velocity, it suggests that this wake distribution is also more notable at higher velocity.

4. Conclusions

This work investigated the energy-harvesting performance of the coupled system consisting of the wavy cylinder and the TMD for the first time. FIV of the wavy cylinder provides the kinetic source while the TMD, with different masses added, renders the utilization of the piezoelectric sheet; as such, output voltage or power can be generated by the coupled system. Experimental measurements, theoretical modeling and CFD simulations were conducted to provide abundant data for analysis and discussion. A wide range of the wavelength (λ_z/D_m = 1.8 ~ 6.0) and wave amplitude (a/D_m = 0.152 ~ 0.25) of the wavy cylinder were considered under three different masses of TMD. The main conclusions drawn from this work are as follows:

1. The performance of the coupled system highly depends on the wavelength and wave amplitude of the wavy cylinder. The maximum output voltage or power is reached by the coupled system when the wavy cylinder has the longest wavelength $\lambda_z/D_m = 6.0$ and the largest wave amplitude $a/D_m = 0.25$. The total output power from the coupled system of this wavy cylinder is 2.21 times that of the baseline smooth cylinder. The behavior of the transversal oscillation of the wavy cylinder echoes the observations made on the harvested energy by the coupled system. On the other hand, when the wavy cylinder has the shortest wavelength $\lambda_z/D_m = 1.8$, energy harnessed by the coupled system is reduced compared to that of the baseline regardless of any wave amplitudes.
2. As for the frequency, the frequencies of all test cases are very closed to the natural frequency of the air bearing system. That is, although the wavy surface can affect the transverse oscillation behavior obviously, its dynamics response still belongs to vortex induced vibration (VIV). With Mass 0 and Mass 2 added in the TMD system, respectively, the lock-in frequency of the coupling system increases very smoothly with reduced velocity, however, when the Mass 1 is applied, there are two dominant frequencies, i.e., f_y/f_N = 0.98 and 1.1 due to the resonance between TMD system and base excitation generated by the oscillation of cylinders.
3. A theoretical model is established, and further validated by experimental results. Results suggest that the output power of TMD has a strong positive correlation with the transverse oscillation and its slope highly depends on the ratio of the FIV frequency and natural frequency

(Mass) of TMD. When the natural frequency of TMD is closed to the FIV frequency, the system can achieve the highest energy extraction performance.

4. CFD simulation results indicate that the wavy surface influences the near wake of cylinder significantly. 3D wakes, such as hairpin vortexes are observed in the downstream of wavy cylinder while 2D wake is discovered along the axis direction of the smooth cylinder. Under the effects of hairpin vortex, narrower and wider wakes occur respectively at the node plane and saddle plane of the worst energy extraction case, i.e., λ_z/D_m=1.8 and a/D_m=0.25, respectively. This wake pattern can lead to a less mean pressure difference of the wavy cylinder than that of the smooth cylinder, produce a less force (FIV oscillation) and further generate less power output. Conversely, for the best harvester case with λ_z/D_m=6.0 and a/D_m=0.25, a significant wider wake is observed at the node plane, with a narrower wake generated at the saddle plane, which can create a larger mean pressure difference and further increase the power output.

Here, the current study did not explicitly address the energy harvesting performance of the fluid-structure interaction (FSI) system through a theoretical analysis. Instead, the primary focus was on the prediction of voltage output for a given base oscillation. While the power output of the system was not directly quantified through theoretical means, the findings of the theorical study offer valuable insights into the energy harvesting performance of the FSI system based on the experimental measurements obtained. Nevertheless, it is necessary to further improve the theoretical model to account for the nonlinearities inherent in the fluid-structure coupled system, which can provide a more comprehensive understanding of the energy harvesting performance of the FSI system.

Acknowledgement

This work is supported by Natural Science Foundation of Guangdong Province through grants 2021A1515010337, National Natural Science Foundation of China (NSFC) through grants 11872018 and 12072382, Shenzhen NSF through grant JCYJ20190807161217754, Research Grants Council of Hong Kong under General Research Fund through grant 15218421 and NSFC through grant 91952107.

Data availability statement

The data that support the findings of this study are available from the corresponding author upon reasonable request.

Appendix A. Derivations of mechanical and electrical equations

The motion of the base for the cantilever, as shown in Fig.3, is represented by $w_b(t)$ relative to the inertial frame of reference *OYZ* and the $w(z, t)$ denotes the effective transverse deflection relative to the base-fixed coordinate *oyz*. Accordingly, the total displacement of the piezo-beam can be written:

$$w_t(z,t) = w(z,t) + w_b(t) \tag{A1}$$

Based on the Generalized Hamilton principle, the governing equations can be derived as follows[10, 33, 44]:

$$\int_0^t (\delta T - \delta V + \delta W)dt{=}0 \tag{A2}$$

where *T, V* and *W* are total kinetic energy, potential energy and the electric energy, respectively. The total kinetic energy of the cantilever beam can be expressed as:

$$T = \frac{1}{2}\int_0^l m_1[\dot{w} + \dot{w}_b]^2 dz + \frac{1}{2}\int_l^L m_2[\dot{w} + \dot{w}_b]^2 dz + \frac{1}{2}M[\dot{w}(L,t) + \dot{w}_b]^2 \tag{A3}$$

where l and L are the length of sheet and beam, respectively; m_1 is the mass per unit length of the piezo-beam and m_2 is the counterparts of the pure-beam part, and the mass M represents mass block attached on the TMD, respectively. The rotational energy of beam and lump mass is not considered in this study. The potential energy of the piezoelectric cantilever is given by:

$$V = \frac{1}{2}\int_0^l EI_1\left(\frac{\partial^2 w}{\partial z^2}\right)^2 dz + \frac{1}{2}\int_l^L EI_2\left(\frac{\partial^2 w}{\partial z^2}\right)^2 dz + \frac{1}{2}\int_{V_p} T_1 S_1 dV_p \tag{A4}$$

where EI_1 and EI_2 are the flexural stiffness of pure beam and piezo-beam, respectively; $T_1 = c_{11}^E(S_1 - d_{31}E_3)$ and $S_1 = -z(\partial^2 w/\, \partial z^2)$ are the stress and strain on the piezoelectric layers, where c_{11}^E is the Young's modulus at constant electric field, d_{31} is the piezoelectric coefficient and $E_3(t) = -V(t)/2t_\mathrm{p}$ is the electric field component (V and t_p are the voltage and thickness of the piezoceramic layer, respectively), and V_p is the volume of piezoelectric layer. The electric energy in this system can be written as:

$$W = \frac{1}{2}\int_{V_p} E_3 D_3 dV_p - R\frac{dQ_3}{dt}Q_3 \tag{A5}$$

where $D_3 = d_{31}T_1 + \varepsilon_{33}^T E_3$ is electrical displacement (ε_{33}^T is permittivity at constant stress). The second term on the RHS of the Eq. (A5) denotes the electrically extracted work, where R is the resistive electrical load of the connected piezoelectric layer, and Q_3 is the electrical charge. Deriving the dynamic equilibrium equation from the Generalized Hamilton's principle (Eq. (A2))[33, 45], the finial undamped mechanical and electrical equations can be described by:

$$m\frac{\partial^2 w}{\partial t^2} + EI\frac{\partial^4 w}{\partial z^4} + \vartheta_p V(t)\left(\frac{d\delta z}{dz} - \frac{d\delta(z-l)}{dz}\right) = -m\frac{\partial^2 w_b}{\partial t^2} - M\frac{\partial^2 w_b}{\partial t^2}\delta(z-L) \tag{A6}$$

$$\vartheta_p \int_0^{\ell} \frac{\partial^3 w}{\partial t \, \partial z^2} - C_p \frac{dV(t)}{dt} = \frac{V(t)}{R} \tag{A7}$$

where m and EI are the equivalent density and bending stiffness terms; ϑ_p is the piezoelectric coupling coefficient and $C_p = \varepsilon_{33}^{S} bl/t_p$ is the internal capacitance of the piezo-layer, where ε_{33}^{S} is permittivity component at constant strain and b is the width of the piezo-beam. $V(t) = RdQ_3/dt$ is the voltage across the piezoelectric layer.

The relevant boundary conditions for the relative motion of the cantilever beam are listed as follows:

$$\begin{cases} w(0,t) = 0 \\ \left.\frac{\partial w(z,t)}{\partial z}\right|_{z=0} = 0 \\ \left.\left(EI \frac{\partial^2 w(z,t)}{\partial z^2}\right)\right|_{z=L} = 0 \\ \left.\left(EI \frac{\partial^3 w(z,t)}{\partial z^3} - M \frac{\partial^2 w(L,t)}{\partial t^2}\right)\right|_{z=L} = 0 \end{cases} \tag{A9}$$

By introducing the viscous air damping and the strain rate damping into the mechanical equation (A6), the damped equation of the beam motion can be written as:

$$m \frac{\partial^2 w}{\partial t^2} + EI \frac{\partial^4 w}{\partial z^4} + c_a \frac{\partial w}{\partial t} + c_s I \frac{\partial^5 w}{\partial t \, \partial z^4} + \vartheta_p V(t) \left(\frac{d\delta z}{dz} - \frac{d\delta(z-l)}{dz}\right) = -m \frac{\partial^2 w_b}{\partial t^2} - c_a \frac{\partial w_b}{\partial t} -$$

$$M \frac{\partial^2 w_b}{\partial t^2} \delta(z-L) \tag{A10}$$

where $c_s I$ and c_a are the strain rate damping term and viscous air damping coefficient of the beam structure. Typically, for the harvesters operating in air, the external damping excitation is negligible in comparison with the inertial excitation of the base [35]. Therefore, the damping excitation term is omitted, and the mechanical equation (A10) becomes:

$$m \frac{\partial^2 w}{\partial t^2} + EI \frac{\partial^4 w}{\partial z^4} + c_a \frac{\partial w}{\partial t} + c_s I \frac{\partial^5 w}{\partial t \, \partial z^4} + \vartheta_p V(t) \left(\frac{d\delta z}{dz} - \frac{d\delta(z-l)}{dz}\right) = -m \frac{\partial^2 w_b}{\partial t^2}$$

$$-M \frac{\partial^2 w_b}{\partial t^2} \delta(z-L) \tag{A11}$$

To get the deformation of the beam, i.e., $w(z,t)$, an analytical formulation is derived for the natural frequencies and associated mode shapes of cantilevered beam with tip mass, i.e., $\phi_n(z)$. Considering linear undamped clamped-free beam obtained by dropping the damping, forcing and nonlinear terms, Eq. (A11) is simplified into:

$$m \frac{\partial^2 w}{\partial t^2} + EI \frac{\partial^4 w}{\partial z^4} = 0 \tag{A12}$$

where m and EI are assumed to be the counterparts of the beam considering the piezoelectric layer is much thinner and softer than the beam.

The lateral displacement of the beam is assumed to be expressible in the form of a finite series of the regular modal shape

$$w(z,t) = \sum_{n=1}^{\infty} \phi_n(z)\eta_n(t) \tag{A13}$$

where $\eta_n(t)$ is the modal coordinate of the beam for the *n*th mode. The vortex induced vibration frequency is around 1.0 Hz in this study. Under various mass added in TMD system, the frequency of system is also about 0.5-1.5Hz. From previous studies[44], it is known that the second or third natural frequency is far larger than the first natural frequency in this system. So, the first natural frequency is in the dominant status. Consequently, only the fundamental mode shape, i.e., $\phi(z)$, is chosen to establish the electro-mechanical coupling equations in the following sections. The resulting differential equation of eigenfunction problem is given by:

$\phi^{(4)}(z) - \lambda^4\phi(z) = 0$ where $\lambda^4 = \frac{mL^4\omega^2}{EI}$, where ω is the undamped natural modal frequency. The general solution of Eq. (A12) can be described by:

$$\phi(z) = A_1\sin \lambda\frac{z}{L} + A_2\cos \lambda\frac{z}{L} + A_3\sinh \lambda\frac{z}{L} + A_4\cosh \lambda\frac{z}{L} \tag{A14}$$

Then, as the associated boundary conditions in Eq. (A9) are induced, it can be obtained as follows:

$$\phi(0) = 0;\ \phi'(0) = 0;\ \phi''(L) = 0;\ EI\phi'''(L) = -M\omega^2\phi(L) \tag{A15}$$

in which ω represents the resonance frequency of the first mode.

By introducing into the boundary conditions Eq. (A15), the eigenvalue of the system λ can be obtained. Replacing A2, A3 and A4 by A1, the Eq. (A14) is simplified as:

$$\phi(z) = A_1[\cos\lambda\frac{z}{L} - \cosh\lambda\frac{z}{L} + \tau(\sin\lambda\frac{z}{L} - \sinh\lambda\frac{z}{L})] \tag{A16}$$

where τ is

$$\tau = \frac{\sin\lambda - \sinh\lambda + \lambda\frac{M}{mL}(\cos\lambda - \cosh\lambda)}{\cos\lambda + \cosh\lambda - \lambda\frac{M}{mL}(\sin\lambda - \sinh\lambda)} \tag{A17}$$

The modal amplitude constant A_1 can be evaluated by satisfying orthogonality relations of the mode, and thus the eigenfunction $\phi(z)$ is obtained.

Substituting Eq.(A13) into Eqs.(A11) and (A7), and applying the orthogonality conditions for the eigenfunction, the mechanical and electrical equations of the cantilever beam in modal coordinate can be obtained with only considering the fundamental mode

$$\ddot{\eta}(t) + 2\zeta\omega\dot{\eta}(t) + \omega^2\eta(t) + \theta_p V(t) = f(t) \tag{A18}$$

$$\frac{V(t)}{R} - \theta_p\dot{\eta}(t) + C_p\frac{dV(t)}{dt} = 0 \tag{A19}$$

where ζ is the mechanical damping ratio, including the effect of both viscous air damping and strain rate damping. $\theta_p = \vartheta_p d\phi(l)/dz$ is the modal electromechanical coupling term. $f(t)$ represents the modal forcing function for a translating base excitation, which is given as follows:

$$f(t) = -m\frac{\partial^2 w_b}{\partial t^2}\int_0^L \phi(z)dz - M\frac{\partial^2 w_b(L,t)}{\partial t^2}\phi(L,t) \tag{A20}$$

More details about the derivation of the electromechanical equations can also be found in the relevant works [10, 33, 35, 36, 44, 46].

Appendix B. Computational-fluid-dynamics simulations (CFD) Validations

The grid- and time- independence tests are conducted for the smooth cylinder with U_r fixed at 5.0, as shown in Table B1. To conduct a mesh independence study, we calculated three different mesh sizes at $\Delta t = 5 \times 10^{-5}$ s, labelled as Mesh 1, Mesh 2, and Mesh 3 in Table B1. We found that the results obtained from the medium mesh (Mesh 2) were similar to those obtained from the fine mesh (Mesh 3). Therefore, to reduce computational costs, we selected Mesh 2. Additionally, we performed a time-step convergence study at three different time steps, $\Delta t = 1 \times 10^{-4}$ s, 5×10^{-5} s, and 1×10^{-5} s, using Mesh 2. In general, when using the middle spatial resolution (i.e., Mesh2: 9.8×10^{5}) and temporal resolution (i.e., $\Delta t = 5 \times 10^{-5}$), the results in terms of transverse displacement are reasonably consistent with each other. To further validate our simulation method, Table B2 shows the numerical and experimental results of the transversal oscillation displacement (A_r/D_m) of various cylinders. Generally, a good agreement is achieved for any cylinders, especially for the smooth cylinder at $U_r = 5.3$. However, it can be found that compared with the experimental results, the wavy cylinders perform better VIV suppression or promotion in numerical results. It may be related with boundaries differences between simulation and experiments. In simulation, periodic boundaries are imposed at both ends of cylinder in which the wavy cylinder is regarded as having repeatable wavy structures with infinite length. However, in practice, the wavy cylinder only has limited number (changing from 3 to 10) of node and saddle due to the limitation of water tunnel in depth. Furthermore, to eliminate the 3D effects, end plates are adopted at each end of the cylinder in experiments. As such, boundary layers are created near the surface of end plates, which also influence the dynamic response of the cylinder. To simulate the real experiments conditions, the calculation cost is very high while it is luckily seen that the general trend is agree with each other well. For example, the wavy cylinder with $\lambda_z = 1.8D_m$ and $a = 0.25D_m$ could suppress the vibration; conversely, the case with $\lambda_z = 6.0D_m$ and $a = 0.25D_m$ promotes the oscillation obviously. That is, the CFD results still can help us understand the dynamic response and the wake of various cylinders.

Table B1 Grid- and time-independent tests for the smooth cylinder with a reduced velocity $U_r = 5.3$ (Conditions for the optimal selection are marked in bold)

Mesh	Mesh1	Mesh2	Mehs3
Grid numbers	6.3×10^5	$\mathbf{9.8\times10^5}$	14.2×10^5
A_r/D_m	0.385	0.407	0.408
Difference in A_r/D_m	2.95%	-	0.25%
Time-step (s) (Δt)	1×10^{-4}	$\mathbf{5\times10^{-5}}$	1×10^{-5}
A_r/D_m	0.396	0.407	0.408
Difference in A_r/D_m	2.7%	-	0.25%

Table B2 The transversal oscillation displacement (A_r/D_m) for the wavy cylinder of different wavelengths and Mass 0 in the coupled system

Cylinder	Normal cylinder	Wavy cylinder	Wavy cylinder
		λ_z=1.8 and $a = 0.25D_m$	λ_z=6 and $a = 0.25D_m$
	$U_r = 5.3$	$U_r = 5.0$	$U_r = 7.6$
A_r/D_m (CFD)	0.407	0.292	0.497
A_r/D_m (Exp.)	0.397	0.310	0.447

To further verify the predictions of our numerical model on the wake flow, we performed additional simulations and compared the results to those observed in a previously published Particle Image Velocimetry (PIV) experiment conducted by [47]. Specifically, we selected the 2S mode and 2P mode for validation, as shown in Fig. S1. Overall, our numerical results and the PIV experiment exhibit consistent vortex patterns, with minor discrepancies attributable to temporal differences between the experiment and simulation.

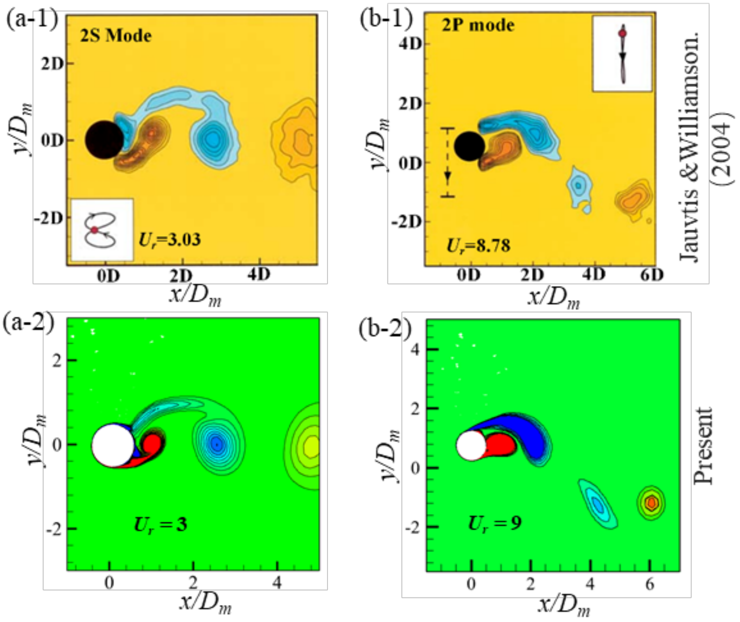

Figure S1. Comparisons of wake patterns for smooth cylinders between the present study and N. Jauvtis and C.H.K. Williamson (a) 2S Mode and (b) 2P Mode

Reference

[1] A. Abdelkefi, "Aeroelastic energy harvesting: A review," *International journal of engineering science,* vol. 100, pp. 112-135, 2016, doi: 10.1016/j.ijengsci.2015.10.006.

[2] M. Hamlehdar, A. Kasaeian, and M. R. Safaei, "Energy harvesting from fluid flow using piezoelectrics: A critical review," *Renewable energy,* vol. 143, pp. 1826-1838, 2019, doi: 10.1016/j.renene.2019.05.078.

[3] J. Wang, L. Geng, L. Ding, H. Zhu, and D. Yurchenko, "The state-of-the-art review on energy harvesting from flow-induced vibrations," *Applied energy,* vol. 267, p. 114902, 2020, doi: 10.1016/j.apenergy.2020.114902.

[4] X. Ma and S. Zhou, "A review of flow-induced vibration energy harvesters," *Energy conversion and management,* vol. 254, p. 115223, 2022, doi: 10.1016/j.enconman.2022.115223.

[5] S.-D. Kwon, "A T-shaped piezoelectric cantilever for fluid energy harvesting," *Applied physics letters,* vol. 97, no. 16, pp. 164102-164102-3, 2010, doi: 10.1063/1.3503609.

[6] Y. Yang, L. Zhao, and L. Tang, "Comparative study of tip cross-sections for efficient galloping energy harvesting," *Applied physics letters,* vol. 102, no. 6, p. 64105, 2013, doi: 10.1063/1.4792737.

[7] F.-R. Liu, H.-X. Zou, W.-M. Zhang, Z.-K. Peng, and G. Meng, "Y-type three-blade bluff body for wind energy harvesting," *Applied physics letters,* vol. 112, no. 23, p. 233903, 2018, doi: 10.1063/1.5029415.

[8] X. He, X. Yang, and S. Jiang, "Enhancement of wind energy harvesting by interaction between vortex-induced vibration and galloping," *Applied physics letters,* vol. 112, no. 3, p. 33901, 2018, doi: 10.1063/1.5007121.

[9] K. Yang, K. Su, J. Wang, J. Wang, K. Yin, and G. Litak, "Piezoelectric wind energy harvesting subjected to the conjunction of vortex-induced vibration and galloping: comprehensive parametric study and optimization," *Smart Mater. Struct,* vol. 29, no. 7, p. 75035, 2020, doi: 10.1088/1361-665X/ab870e.

[10] D. Zhao, X. Hu, T. Tan, Z. Yan, and W. Zhang, "Piezoelectric galloping energy harvesting enhanced by topological equivalent aerodynamic design," *Energy Conversion and Management,* vol. 222, p. 113260, 2020.

[11] J. Wang *et al.*, "Hybrid wind energy scavenging by coupling vortex-induced vibrations and galloping," *Energy conversion and management,* vol. 213, p. 112835, 2020, doi: 10.1016/j.enconman.2020.112835.

[12] S. Jeon, W. Sun, H. Jang, and J. Seok, "Adaptive wind energy harvester with transformable bluff body," *Energy conversion and management,* vol. 238, p. 114159, 2021, doi: 10.1016/j.enconman.2021.114159.

[13] G. Hu, K. T. Tse, K. C. S. Kwok, J. Song, and Y. Lyu, "Aerodynamic modification to a circular cylinder to enhance the piezoelectric wind energy harvesting," *Applied physics letters,* vol. 109, no. 19, p. 193902, 2016, doi: 10.1063/1.4967497.

[14] G. Hu, K. T. Tse, and K. C. S. Kwok, "Aerodynamic mechanisms of galloping of an inclined square cylinder," *Journal of wind engineering and industrial aerodynamics,* vol. 148, pp. 6-17, 2016, doi: 10.1016/j.jweia.2015.10.011.

[15] G. Hu, K. T. Tse, M. Wei, R. Naseer, A. Abdelkefi, and K. C. S. Kwok, "Experimental investigation on the efficiency of circular cylinder-based wind energy harvester with different rod-shaped attachments," *Applied energy,* vol. 226, pp. 682-689, 2018, doi: 10.1016/j.apenergy.2018.06.056.

[16] J. Song, G. Hu, K. T. Tse, S. W. Li, and K. C. S. Kwok, "Performance of a circular

cylinder piezoelectric wind energy harvester fitted with a splitter plate," *Applied physics letters,* vol. 111, no. 22, p. 223903, 2017, doi: 10.1063/1.5008918.

[17] J. Wang, S. Zhou, Z. Zhang, and D. Yurchenko, "High-performance piezoelectric wind energy harvester with Y-shaped attachments," *Energy conversion and management,* vol. 181, pp. 645-652, 2019, doi: 10.1016/j.enconman.2018.12.034.

[18] J. Wang *et al.*, "Exploring the potential benefits of using metasurface for galloping energy harvesting," *Energy conversion and management,* vol. 243, p. 114414, 2021, doi: 10.1016/j.enconman.2021.114414.

[19] H. Kim, J. Lee, and J. Seok, "Novel piezoelectric wind energy harvester based on coupled galloping phenomena with characterization and quantification of its dynamic behavior," *Energy Conversion and Management,* vol. 266, p. 115849, 2022/08/15/ 2022, doi: https://doi.org/10.1016/j.enconman.2022.115849.

[20] A. Ahmed and B. Bays-Muchmore, "Transverse flow over a wavy cylinder," *Physics of fluids. A, Fluid dynamics,* vol. 4, no. 9, pp. 1959-1967, 1992, doi: 10.1063/1.858365.

[21] P. Bearman, & Owen, J. (1998). REDUCTION OF BLUFF-BODY DRAG AND SUPPRESSION OF VORTEX SHEDDING BY THE INTRODUCTION OF WAVY SEPARATION LINES. Journal of Fluids and Structures, 12(1), 123-130., doi: -10.1006/jfls.1997.0128.

[22] K. Lam and Y. F. Lin, "Effects of wavelength and amplitude of a wavy cylinder in cross-flow at low Reynolds numbers," *J. Fluid Mech,* vol. 620, pp. 195-220, 2009, doi: 10.1017/S0022112008004217.

[23] K. Lam, Y. F. Lin, L. Zou, and Y. Liu, "Numerical study of flow patterns and force characteristics for square and rectangular cylinders with wavy surfaces," *Journal of fluids and structures,* vol. 28, pp. 359-377, 2012, doi: 10.1016/j.jfluidstructs.2011.11.006.

[24] Y. F. Lin, H. L. Bai, M. M. Alam, W. G. Zhang, and K. Lam, "Effects of large spanwise wavelength on the wake of a sinusoidal wavy cylinder," *Journal of fluids and structures,* vol. 61, pp. 392-409, 2016, doi: 10.1016/j.jfluidstructs.2015.12.004.

[25] H. L. Bai, B. Zang, and T. H. New, "The near wake of a sinusoidal wavy cylinder with a large spanwise wavelength using time-resolved particle image velocimetry," *Experiments in fluids,* vol. 60, no. 1, pp. 1-18, 2019, doi: 10.1007/s00348-018-2664-3.

[26] H. L. Bai, M. M. Alam, N. Gao, and Y. F. Lin, "The near wake of sinusoidal wavy cylinders: Three-dimensional POD analyses," *The International journal of heat and fluid flow,* vol. 75, pp. 256-277, 2019, doi: 10.1016/j.ijheatfluidflow.2019.01.013.

[27] K. Zhang, H. Katsuchi, D. Zhou, H. Yamada, T. Zhang, and Z. Han, "Numerical simulation of vortex induced vibrations of a flexibly mounted wavy cylinder at subcritical Reynolds number," *Ocean engineering,* vol. 133, pp. 170-181, 2017, doi: 10.1016/j.oceaneng.2016.11.025.

[28] G. R. S. Assi and P. W. Bearman, "Vortex-induced vibration of a wavy elliptic cylinder," *Journal of fluids and structures,* vol. 80, pp. 1-21, 2018, doi: 10.1016/j.jfluidstructs.2018.02.007.

[29] Y. Cha, H. Kim, and M. Porfiri, "Energy harvesting from underwater base excitation of a piezoelectric composite beam," *Smart materials and Structures,* vol. 22, no. 11, p. 115026, 2013.

[30] T. Tan, Z. Yan, and M. Hajj, "Electromechanical decoupled model for cantilever-beam piezoelectric energy harvesters," *Applied Physics Letters,* vol. 109, no. 10, p. 101908, 2016.

[31] A. M. Wickenheiser, T. Reissman, W.-J. Wu, and E. Garcia, "Modeling the effects of electromechanical coupling on energy storage through piezoelectric energy harvesting," *IEEE/ASME Transactions on Mechatronics,* vol. 15, no. 3, pp. 400-411, 2009.

[32] J. J. Connor, *Structural motion control*. Pearson Education, Inc New York, NY, USA, 2003.

[33] A. Aladwani, O. Aldraihem, and A. Baz, "A Distributed Parameter Cantilevered Piezoelectric Energy Harvester with a Dynamic Magnifier," *Mechanics of advanced materials and structures,* vol. 21, no. 7, pp. 566-578, 2014, doi: 10.1080/15376494.2012.699600.

[34] A. Erturk and D. J. Inman, "An experimentally validated bimorph cantilever model for piezoelectric energy harvesting from base excitations," *Smart materials and structures,* vol. 18, no. 2, pp. 025009-025009 (18), 2009, doi: 10.1088/0964-1726/18/2/025009.

[35] A. Erturk and D. J. Inman, "An experimentally validated bimorph cantilever model for piezoelectric energy harvesting from base excitations," *Smart materials and structures,* vol. 18, no. 2, p. 025009, 2009.

[36] T. Tan, Z. Yan, and M. Hajj, "Electromechanical decoupled model for cantilever-beam piezoelectric energy harvesters," *Applied physics letters,* vol. 109, no. 10, pp. 79-82, 2016, doi: 10.1063/1.4962533.

[37] A. Khalak and C. H. K. Williamson, "MOTIONS, FORCES AND MODE TRANSITIONS IN VORTEX-INDUCED VIBRATIONS AT LOW MASS-DAMPING," *Journal of fluids and structures,* vol. 13, no. 78, pp. 813-851, 1999.

[38] P. R. F. Teixeira and A. M. Awruch, "Numerical simulation of fluid–structure interaction using the finite element method," *Computers & fluids,* vol. 34, no. 2, pp. 249-273, 2005, doi: 10.1016/j.compfluid.2004.03.006.

[39] B. Zhang, B. Song, Z. Mao, W. Tian, and B. Li, "Numerical investigation on VIV energy harvesting of bluff bodies with different cross sections in tandem arrangement," *Energy (Oxford),* vol. 133, pp. 723-736, 2017, doi: 10.1016/j.energy.2017.05.051.

[40] P. Han, G. Pan, and W. Tian, "Numerical simulation of flow-induced motion of three rigidly coupled cylinders in equilateral-triangle arrangement," *Physics of fluids (1994),* vol. 30, no. 12, p. 125107, 2018, doi: 10.1063/1.5054333.

[41] W. Wang and F. Zhao, "Numerical investigation on flow-induced vibration response of the cylinder inspired by the honeycomb," *Ocean Engineering,* vol. 268, p. 113461, 2023/01/15/ 2023, doi: https://doi.org/10.1016/j.oceaneng.2022.113461.

[42] S. Martini, M. Morgut, and R. Pigazzini, "Numerical VIV analysis of a single elastically-mounted cylinder: Comparison between 2D and 3D URANS simulations," *Journal of fluids and structures,* vol. 104, p. 103303, 2021, doi: 10.1016/j.jfluidstructs.2021.103303.

[43] A. A. Wray, P. Moin, and J. C. R. Hunt, "Eddies, streams, and convergence zones in turbulent flows," ed, 1988.

[44] S. G. Kelly, *Mechanical vibrations : theory and applications*. Stamford, CT: Stamford, CT : Cengage Learning, 2012.

[45] L. Meirovitch and R. Parker, "Fundamentals of vibrations," *Appl. Mech. Rev.,* vol. 54, no. 6, pp. B100-B101, 2001.

[46] P. Łabędzki, R. Pawlikowski, and A. Radowicz, "Transverse vibration of a cantilever beam under base excitation using fractional rheological model," in *AIP Conference Proceedings*, 2018, vol. 2029, no. 1: AIP Publishing LLC, p. 020034.

[47] N. a. Jauvtis and C. Williamson, "The effect of two degrees of freedom on vortex-induced vibration at low mass and damping," *Journal of Fluid Mechanics,* vol. 509, pp. 23-62, 2004.